

**DETERMINATION OF FLAME CHARACTERISTICS IN  
A LOW SWIRL BURNER AT GAS TURBINE  
CONDITIONS THROUGH REACTION ZONE IMAGING**

A Dissertation  
Presented to  
The Academic Faculty

by

Karthik Periagaram

In Partial Fulfillment  
of the Requirements for the Degree  
Doctor of Philosophy in the  
Guggenheim School of Aerospace Engineering

Georgia Institute of Technology  
December 2012

# TABLE OF CONTENTS

<b>List of Figures</b>	<b>v</b>
<b>List of Tables</b>	<b>vi</b>
<b>List of Symbols</b>	<b>vii</b>
<b>Summary</b>	<b>viii</b>
<b>1 Introduction</b>	<b>1</b>
1.1 Motivation . . . . .	2
1.2 Literature Review . . . . .	7
1.2.1 Low Swirl Burner . . . . .	7
1.2.2 CH PLIF Implementations . . . . .	8
<b>2 Background</b>	<b>10</b>
2.1 LSB Flow Field . . . . .	10
2.2 LSB Flame Stabilization . . . . .	10
2.3 CH PLIF Signal Modeling . . . . .	10
2.3.1 Basic Model . . . . .	10
2.3.1.1 Absorption Integral Calculation . . . . .	13
2.3.1.2 Population Distribution . . . . .	14
2.3.1.3 Solution . . . . .	14
2.3.2 CH PLIF Process . . . . .	15
2.3.3 Improved Model . . . . .	20
2.3.3.1 Absorption Integral Calculation . . . . .	23
2.3.3.2 Population Distribution . . . . .	24

2.3.3.3	Solution . . . . .	25
<b>3</b>	<b>Experimental Methods and Considerations</b>	<b>26</b>
3.1	LSB Configurations . . . . .	26
3.1.1	Configuration A . . . . .	27
3.1.1.1	Test Facility . . . . .	27
3.1.1.2	Low Swirl Burner . . . . .	29
3.1.2	Configuration B . . . . .	30
3.1.2.1	Test Facility . . . . .	31
3.1.2.2	Low Swirl Burner . . . . .	34
3.2	Diagnostics . . . . .	34
3.2.1	Laser Doppler Velocimetry . . . . .	34
3.2.2	CH* Chemiluminescence . . . . .	37
3.2.2.1	Image Processing . . . . .	37
3.2.3	CH Planar Laser-Induced Fluorescence . . . . .	40
3.2.3.1	Imaging System . . . . .	42
3.2.3.2	Laminar Flame Setup . . . . .	42
3.2.3.3	Laser Wavelength Calibration . . . . .	43
<b>4</b>	<b>CH PLIF Signal Modeling and Validation</b>	<b>46</b>
4.1	CH PLIF Preliminary Experiments . . . . .	46
4.1.1	Excitation Scan . . . . .	46
4.1.2	Linearity Test . . . . .	49
4.2	Fluorescence Signal Modeling . . . . .	51
4.3	Results . . . . .	59
<b>5</b>	<b>LSB Flame Characteristics</b>	<b>60</b>
5.1	Effect of Reference Velocity . . . . .	60
5.2	Effect of Preheat Temperature . . . . .	62

5.3	Effect of Swirler Vane Angle . . . . .	64
5.4	Effect of Equivalence Ratio . . . . .	65
5.5	Effect of Combustor Pressure . . . . .	66
5.6	Flame Structure . . . . .	67
<b>6</b>	<b>Conclusions</b>	<b>68</b>
<b>A</b>	<b>Seeder Design</b>	<b>69</b>
	<b>References</b>	<b>73</b>

# LIST OF FIGURES

2.1	Transitions in a basic two-level model for fluorescence . . . . .	11
2.2	CH $B^2\Sigma^- \leftarrow X^2\Pi$ (0,0) R-bandhead absorption lines . . . . .	16
2.3	Potential curves for electronic energy levels in the CH molecule . . . . .	19
2.4	Relevant transitions in a CH molecule . . . . .	20
2.5	Transitions in the improved CH fluorescence model . . . . .	21
3.1	Schematic of test facility A . . . . .	28
3.2	Detail schematic of configuration A . . . . .	30
3.3	Schematic of test facility B . . . . .	31
3.4	Detail schematic of configuration B . . . . .	33
3.5	Schematic of the LDV setup . . . . .	35
3.6	Sample CH* chemiluminescence data . . . . .	38
3.7	Schematic of the alexandrite laser . . . . .	41
3.8	Schematic of the laser calibration experiment . . . . .	43
3.9	Results of the laser calibration experiment . . . . .	44
4.1	Schematic of the excitation scan experiment . . . . .	47
A.1	Schematic of the old seeder design . . . . .	70
A.2	Schematic of the new seeder design . . . . .	71

# LIST OF TABLES

3.1	Swirler Dimensions . . . . .	27
4.1	Einstein A coefficients . . . . .	51
4.2	Quenching Cross-sections . . . . .	52
4.3	Einstein B coefficientsFIXME . . . . .	54
4.4	Spectroscopic constants . . . . .	56

## LIST OF SYMBOLS

$X_f$  Flame standoff distance

## SUMMARY



## CHAPTER 1

1

## INTRODUCTION

2

The need to reduce pollutant emissions, particularly the oxides of nitrogen,  $\text{NO}_x$ , is driven by increasing ecological awareness and stringent government regulations. This spurs efforts in the gas turbine industry to seek cleaner, more environment-friendly combustion concepts. Several mechanisms have been identified to explain the production of  $\text{NO}_x$  in hydrocarbon-air combustion systems. Of these, the thermal  $\text{NO}_x$  mechanism discovered by Zel'dovich, is a prominent source of  $\text{NO}_x$  production at the high temperature conditions encountered in typical combustors. The amount of thermal  $\text{NO}_x$  produced scales exponentially with the adiabatic flame temperature.

Efforts to reduce the flame temperature have led low  $\text{NO}_x$  gas turbines to adopt one of two options—Lean Premixed (LP) operation, or Rich-Quench-Lean (RQL) operation. Of these, RQL combustion suffers from sooting issues during the rich combustion step and the requirement of a second mixing event during the quenching step. Incomplete mixing can result in stoichiometric combustion in localized pockets within the combustor. LP combustion, on the other hand, is conceptually simpler and avoids the formation of such high temperature zones. Further, it entails operating at low equivalence ratios, reducing the temperature in the combustion zone. In practice, 1800 K is considered a limiting value for the flame temperature, ensuring that the thermal  $\text{NO}_x$  production is constrained to a minimum.

Operating a combustor at such lean conditions results in weaker combustion processes that are highly susceptible to perturbations and results in combustor instabilities or even flame blow off. This highlights the requirement for robust flame stabilization techniques that can sustain combustion at ultra-lean conditions. In their most basic form, flame stabilization techniques work by making the local reactant

velocity and the local flame speed equal. In the context of lean flames, the risk is of the slowly propagating flames to be blown off by the high velocity reactant stream. Consequently, flame stabilization in gas turbine combustion is brought about either by reducing the local reactant velocity (e.g. by using bluff body flame holders), by boosting the local flame velocity (e.g. by enhancing product recirculation), or by providing continual ignition to the flame (e.g. by using pilot flames).

Swirl-stabilized combustion is a widely used flame stabilization technique in gas turbine applications.[1,2] It primarily functions by inducing recirculation zones in the flow field that transport heat and radicals from the products into the reactants. This enhances the flame propagation velocity by increasing reaction rates within the flame, resulting in robust flame stabilization. However, the recirculation zones increase the peak residence times of the products and cause more thermal  $\text{NO}_x$  to be produced in the combustor. Nevertheless, swirl-stabilized combustors are ubiquitously employed today in land-based gas turbines used for power generation.

More recent research[3] on the Low Swirl Burner (LSB) has identified a potential solution for this problem. The LSB anchors a lifted flame, reducing the need for high swirl in the flow field. The lifted, V-shaped flame is stabilized by aerodynamic means which allows for robust operation even at low equivalence ratios. This weakens the recirculation zones and eliminates pockets of high residence times, resulting in significantly reduced  $\text{NO}_x$  emissions compared to a similar high-swirl design.

## 1.1 Motivation

By comparison to atmospheric pressure experiments, high pressure experimental testing of combustion systems is fraught with difficulties. This is reflected in the comparatively smaller subset of papers that report experimental results from high pressure tests. The primary source of these difficulties stems from the need for complicated testing facilities to reach and maintain high pressures. The inherently limited access

afforded by pressure vessels makes intrusive methods of data gathering nearly impos- 52  
sible. As a result, any need for spatially resolved data other than temperature and 53  
pressure measurements has to be met by optical diagnostics. 54

In the context of LSB research, these difficulties have confined much of the pub- 55  
lished experimental results to ambient conditions. The eventual application of this 56  
technology in gas turbine engines requires high quality data acquired at high pressure 57  
conditions. Ideally, such data will map the velocity field and heat release in the LSB 58  
and study their variation with flow conditions. Since the LSB relies on the velocity 59  
field to stabilize its flame, its flame characteristics hold information pertinent to both 60  
the velocity field and the heat release distribution within the combustor. This allows 61  
a passive diagnostic such as recording the flame chemiluminescence to be used even 62  
at high pressure conditions to observe and record usable data about the LSB flame 63  
characteristics. Such data, acquired at conditions closer to real world gas turbine 64  
combustor operating conditions is of particular interest to the gas turbine industry. 65

The primary flame characteristic of interest is the flame standoff distance, defined 66  
as the distance from the flame stabilization point to the inlet of the LSB. This met- 67  
ric is useful is gauging the stability of the flame and the need for control systems 68  
to closely monitor its tendency to flashback or blow-off. The standoff distance also 69  
relates to the heat load experienced by the injector and consequently affects how of- 70  
ten the mechanical components of the LSB will required to be replaced in operation. 71  
Finally, a systemic variation in the location of the flame over a range of flow parame- 72  
ters may indicate potential problems operating the combustor at previously untested 73  
conditions. 74

Quantifying the shape of the flame can complement the information gleaned from 75  
the flame standoff measurements. In case of the V-shaped LSB flame, this can be 76  
conveniently obtained by measuring the angle of the flame cone. Changes in the flame 77  
angle affect the length of the flame, which is a design consideration for sizing LSB 78

combustors in gas turbines.

The profile of the flame chemiluminescence along the length of the combustion zone is representative of the local heat release at those locations. A uniform heat release profile is preferred so as to avoid thermally stressing the combustor at the hot spots. Further, since  $\text{NO}_x$  production rates are so strongly dependent on temperature, the heat release profile can help forecast emissions performance issues of the combustor, particularly when augmented by knowledge of the local flow velocity (and hence, residence time). Finally, the heat release map could be incorporated into  $n$ - $\tau$  models to predict the onset of thermo-acoustic instabilities in the combustor.

The primary goal of this research work is to study the flame characteristics of the LSB, such as its location and shape, as a means to learn more about the combustor operation at high pressure conditions.

In case of lean hydrocarbon flames, the primary sources of flame chemiluminescence are  $\text{OH}^*$  ( $A^2\Sigma^+ \rightarrow X^2\Pi$  bands, 310 nm),  $\text{CH}^*$  ( $A^2\Delta \rightarrow X^2\Pi$  bands, 430 nm,  $B^2\Sigma^- \rightarrow X^2\Pi$  bands, 390 nm),  $\text{C}_2^*$  ( $d^3\Pi \rightarrow a^3\Pi$  Swan bands, 470 nm, 550 nm) and the  $\text{CO}_2^*$  (band continuum, 320–500 nm). Of these,  $\text{CH}^*$  chemiluminescence has several advantages that make it suitable for this particular study. First, collection of  $\text{CH}^*$  chemiluminescence is less affected by blackbody radiation from the walls of the combustor, compared to longer wavelength emissions from a species like  $\text{C}_2^*$ . Its narrow bandwidth allows one to use a bandpass filter to collect signals from only the wavelengths of interest, further minimizing interference from other light sources. Using such a narrow bandpass filter for a broad band emitter like  $\text{CO}_2^*$  would result in rejecting most of the available signal.  $\text{CH}^*$  chemiluminescence occurs in the visible wavelengths and does not require expensive UV lenses to acquire—as would be necessary to image  $\text{OH}^*$  chemiluminescence, for instance. In typical LSB operation, where the flame is not expected to operate near extinction,  $\text{CH}^*$  chemiluminescence can serve as a reliable indicator of heat release in the combustor. For all these reasons,

CH\* chemiluminescence is a suitable technique to image the LSB flame. 106

Ultimately, the amount of information that can be gathered by imaging the flame 107  
chemiluminescence is limited by its spatial resolution. Since chemiluminescence imag- 108  
ing is integrated over the line of sight, studying the flame brush or the flame structure 109  
is beyond its capabilities. A planar imaging technique such as Planar Laser-Induced 110  
Fluorescence (PLIF) is better suited for such applications. 111

In hydrocarbon flames, species accessible to PLIF are generally minor species in 112  
the flame. PLIF studies of hydrocarbon flames have hitherto focused on the OH 113  
radical. However, OH is produced in the flame zone and destroyed by relatively slow 114  
three-body reactions, causing it to persist and be transported away from the flame 115  
and into the product zone.[4] As a result, it does not serve as a direct marker of the 116  
flame front. Instead, the location of the flame is inferred from the sharp gradient in 117  
the OH signal as the reactants are converted into products. 118

The persistence of OH in the products makes OH PLIF somewhat less suited to 119  
studying flames in flows with high product recirculation. In such flows, the presence 120  
of OH in both the reactants and the products weakens the gradient at the flame. 121  
Further, since OH radicals could be transported transverse to the flame, its presence 122  
or absence serves as an unreliable indicator of local flame extinctions. Nevertheless, 123  
researchers have been able to use OH PLIF successfully[5, 6] to study such flames, 124  
particularly when the images are enhanced by nonlinear filtering techniques.[7, 8] 125

This study utilizes CH PLIF as the flame visualization technique. CH is produced 126  
and destroyed rapidly by fast two-body reactions, confining it to the thin heat release 127  
zone of the flame. This makes it suitable for use as a marker species for the flame 128  
front.[9] CH is formed during the breakup of hydrocarbon fuel molecules[10] and is 129  
also known to play an important role in the production of prompt NO<sub>x</sub>. [11] Hence, it 130  
is a minor species of considerable importance to combustion research. This leads us 131  
to the second motivation for this study—to examine the use of CH PLIF as a flame 132

imaging technique in combustion systems and further, to use it to image and study  
the LSB flame.

The use of CH PLIF to study lean hydrocarbon flames has been difficult in the past  
due to several issues. First, the concentration of the CH species in hydrocarbon flames  
rapidly declines with equivalence ratio, making high quality imaging of the flame front  
at lean conditions challenging. Further, the implementation techniques in the past  
have suffered from a host of problems ranging from elastic scattering interference  
to saturation issues leading to diminished signal-to-noise ratios. However, a recent  
implementation by Li et al.[12] has managed to overcome these issues and has been  
demonstrated to image lean flames with good fidelity.

Recent studies[13] have indicated that the species HCO is a superior indicator  
of heat release in hydrocarbon flames when compared to CH or OH. The HCO LIF  
signal has been demonstrated to correlate well with the heat release rate, with little  
dependence on equivalence ratio or strain rate. The last factor, in particular, has  
been shown to quench the CH PLIF signal[14] in highly strained flames, even when  
the flame itself is not extinguished. Unfortunately, the signal levels from HCO LIF  
are very poor[13, 15] and are unsuitable for single-shot investigation of hydrocarbon  
flames. To overcome this, one study[15] proposed a simultaneous LIF investigation of  
 $\text{CH}_2\text{O}$  and OH with the reasoning that the formation rate of HCO is governed directly  
by the product of the concentration of these two intermediates. This method has been  
used in a number of investigations,[16] despite being experimentally cumbersome.  
A more recent implementation[17] has demonstrated single-shot HCO PLIF with  
moderate signal-to-noise ratios by utilizing a novel excitation scheme. Follow up  
studies applying this technique in other hydrocarbon flames are awaited.

## 1.2 Literature Review

157

### 1.2.1 Low Swirl Burner

158

The LSB is a relatively new combustion technology and as such has a brief history. 159  
Initial interest in low swirl combustion was primarily motivated by its ability to sta- 160  
bilize a freely propagating turbulent flame.[18] As a result, initial designs of the LSB 161  
(which at the time used tangential jets to produce swirl) were pursued by Bédard and 162  
Cheng[3, 19] as test beds for studying 1-D, planar turbulent flames. Several subse- 163  
quent studies[20–26] utilized this behavior and investigated fundamental turbulent 164  
flame structure and propagation in the jet LSB. Simultaneously, the discovery of its 165  
low  $\text{NO}_x$  emissions prompted interest in commercial applications of the LSB, such as 166  
in industrial furnaces and boilers.[27–29] 167

The current form of the LSB (as used in this thesis) using vanes to generate swirl 168  
was originally modified from a typical production swirl injector used in gas turbine 169  
combustors. The results of testing this new design were published by Johnson et 170  
al.[30] The design elements of the new injector—now called the Low Swirl Injector 171  
(LSI)—were tweaked in an atmospheric pressure test rig using LBO and flame location 172  
as the criteria. The atmospheric tests were conducted with preheated reactants at 173  
up to 650 K. The more interesting results from the work came from high pressure, 174  
high preheat tests (15 atm, 700 K) in a test rig with limited optical access. The 175  
researchers measured a dramatic (50%) reduction in the  $\text{NO}_x$  emissions by switching 176  
from the original (“High” Swirl Injector) to the new low swirl design. The emissions 177  
performance was also noted by Nazeer et al.[31] 178

Subsequent studies by Cheng et al.[32,33] explored the characteristic velocity field 179  
in the LSB using PIV and discovered self-similar behavior that implied that the flame 180  
location was unaffected by the mass flow rate of the reactants. This led to further 181  
insights into the flame stabilization mechanism used by the LSB. These results will 182

be revisited in Chapter 2 in finer detail.

The effects of using an enclosure to contain the combustion zone were explored by Cheng et al.[34] who found scaling criteria for minimizing the effect of the enclosure on the flame stabilization location.

More recent work has tended to focus on the use of various fuels such as hydrogen mixtures[35] with and without dilution[36], landfill gas[33, 37] and syngas[38].

Relatively little research has focused on the flame location and other characteristics and studied their variation at gas turbine relevant conditions. Notably, Petersson et al.[39] used a different modified version of the LSB that had fewer vanes compared to the one tested by Cheng and co-workers, and used a bevy of techniques to study the turbulent flame. In particular, they used OH PLIF to image a non-preheated, atmospheric flame at low flow rates. While their motivation was to develop a detailed database to compare and validate LES models, it remains one of the few works that shows the structure of the LSB flame with good spatial resolution.

### 1.2.2 CH PLIF Implementations

Historically, CH was the first species to be detected using LIF in a flame.[40] Early attempts[41, 42] to excite the CH layer used variations of short-pulsed, YAG-pumped dye laser output targeting transitions in one branch of the  $A^2\Delta \leftarrow X^2\Pi$  (0,0) band and observing resulting fluorescence in the same band, but at a different rotational branch. These methods relied on the strong absorption of the  $A-X$  bands to generate high signal values, but suffered from interference from elastic scattering. Further, the short pulsewidth and narrow spectral bandwidths of the excitation sources quickly saturated the transition being pumped, limiting the amount of LIF signal measured.

Namazian et al.[43] and Schefer et al.[44] had better success at overcoming interference issues by exciting the  $A-X$  (0,0) band, but observing fluorescence from the (0,1) band. Another similarly non-resonant technique was proposed by Paul et al.[45]



who excited the  $A^2\Delta \leftarrow X^2\Pi$  (1,0) band and observed resulting fluorescence from the (1,1) and (0,0) bands. These approaches provide good separation between the excitation and emission wavelengths, but are hampered by the spectroscopic properties of the CH system—which will be explored further in Section 2.3.2—which disfavor radiative transitions in the non-diagonal (0,1) or (1,0) bands. Further, Namazian et al.’s scheme suffers from interference due to Raman scattering of the excitation beam due to the fuel species overlapping the (0,1) band.

Carter and several others[46–54] pumped the  $B^2\Sigma^- \leftarrow X^2\Pi$  (0,0) band and utilized fast electronic transfer from the  $B^2\Sigma^-$ ,  $v = 0$  to populate the  $A^2\Delta$ ,  $v = 0, 1$  levels. This way, they could observe the strong emission from  $A^2\Delta \rightarrow X^2\Pi$  (1,1) and (0,0) bands. This method overcame the interference issues by providing sufficient spacing between the excitation and emission wavelengths, but suffered from saturation issues due to the short pulsewidth of the excitation sources. Further, at high laser irradiance, the group recorded noticeable interference from fuel LIF.

Li et al.[12, 55, 56] investigated using an alexandrite laser[57] to improve upon the previous excitation scheme by targeting the R-bandhead of the  $B^2\Sigma^- \leftarrow X^2\Pi$  (0,0) transition with a long pulsed excitation beam. This excitation scheme offers several advantages over previous implementations. First, it inherits the large spacing between the excitation and emission wavelengths and reduced interference issues from Carter et al.’s implementation. Next, by using a long pulsed laser beam, it overcomes saturation issues. In fact, the researchers note that the pulsewidth is long enough to allow the same CH molecule to go through the excitation-deexcitation sequence several times, boosting signal output. This aspect of the implementation is further enhanced if the laser is operated in multimode, with a large spectral bandwidth, allowing the laser to target several lines near the R-bandhead. The resultant improvement in signal-to-noise makes this technique suitable to study even low equivalence ratio hydrocarbon flames. This is the excitation scheme that is used in this study.

## CHAPTER 2

236

## BACKGROUND

237

### 2.1 LSB Flow Field

238

### 2.2 LSB Flame Stabilization

239

### 2.3 CH PLIF Signal Modeling

240

While the intent and scope of this work is to use CH PLIF as a visualization technique 241  
to image the flame front with high fidelity, it would be extremely useful to be able 242  
to predict the CH PLIF signal intensity for different reactant mixtures and initial 243  
conditions as a means to gauge the feasibility of applying the technique to acquire 244  
high fidelity images of the flame at those conditions. To that end, this discussion 245  
will attempt to develop a mathematical model to calculate, in a semi-quantitative 246  
manner, the rate of CH PLIF photons emitted by the illuminated reaction zone. The 247  
following discussion introduces important concepts in LIF signal intensity calculation 248  
using a simple two-level model and then proceeds to apply these concepts to model 249  
the more complicated physical processes in the CH system. 250

#### 2.3.1 Basic Model

251

In its most basic form, the number of fluorescence photons generated in a system,  $\Phi$  is 252  
the product of the number of emitters,  $N$  and the Einstein coefficient for spontaneous 253  
emission,  $A$ . 254

$$\Phi = N \times A \quad (2.1)$$

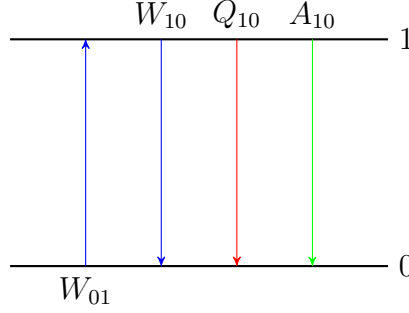


Figure 2.1: The figure shows energy levels and transitions between two levels, labeled 0 and 1, in a basic model of laser-induced fluorescence. Stimulated absorption and emission are shown in *blue*, collisional quenching is shown in *red* and spontaneous emission is shown in *green*.

The fluorescence photons produced are radiated in all directions and only a fraction of these can be recorded by a collection system in an experiment. This fraction is determined by the experimental set up, the collection angle, and the efficiency of the optics and the detector used to record the signal. For this analysis, however, this fraction is omitted to reduce complexity.

In a simple two-level model for the fluorescing system, as shown in Figure 2.1, Equation 2.1 may be expanded in terms of the number density of the emitters,  $n$ , and the volume in which the fluorescence occurs,  $V$ .

$$\Phi = n_1 V A_{10} \quad (2.2)$$

The population of the upper state,  $n_1$  can be solved for by rate analysis. The mathematical treatment is not particularly complicated and is covered in detail by various textbooks and review papers.[58, 59] Here, we shall merely remark that the functional form of the solution has two limiting cases. The limits are decided by the relative magnitudes of the pumping rate,  $W_{01}$ , and the relaxation rate given by the sum of the spontaneous emission rate and the collisional quenching rate,  $A_{10} + Q_{10}$ . The former is the rate at which the upper energy level is populated through absorption. The latter represents the rate at which the molecules return to the

lower energy state, either through spontaneous emission or by losing energy to other molecules through inelastic collisions.

When the pumping rate is far lower compared to the relaxation processes ( $W_{01} \ll A_{10} + Q_{10}$ ), the solution tends to the weak excitation limit. In this limit, the functional form of the solution is shown in Equation 2.3

$$\Phi = n_0 V W_{01} \frac{\overbrace{A_{10}}^{\text{Fluorescence Yield}}}{A_{10} + Q_{10}} \quad (2.3)$$

The  $n_0 V W_{01}$  term in Equation 2.3 represents the number of molecules that are excited to the upper state per second, while the fluorescence yield represents the fraction of these molecules that will produce a LIF signal. In typical combustion environments, the fluorescence yield is usually small, since the collisional quenching rate dominates the spontaneous emission rate. The rate of collisional quenching of the marker species by another species in the flame is proportional to the frequency of collisions between the two species. Further, the effectiveness of such collisions is decided by a collision cross-section,  $\sigma$ , which is often a function of the temperature. Equation 2.4 presents the calculation of the collisional quenching rate by summation over all the species,  $i$ , in the flame.

$$\begin{aligned} Q_{10} &= \sum_i n_i \times \sigma_i \times c_i \\ &= \sum_i n_i \sigma_i \sqrt{\frac{8kT}{\pi \mu_i}} \\ &= \sqrt{\frac{8kT}{\pi}} \sum_i \frac{n_i \sigma_i}{\sqrt{\mu_i}} \end{aligned} \quad (2.4)$$

In Equation 2.4,  $k$  is the Boltzmann constant,  $T$  is the local temperature,  $n_i$  is the number density of species  $i$  and  $\mu_i$  represents the reduced mass of the colliding

molecules, given by Equation 2.5.

288

$$\mu_i = \frac{m_i m}{m_i + m} \quad (2.5)$$

In Equation 2.5,  $m$  is the mass of the marker species, while  $m_i$  are the masses of the colliding species. Since LIF in combustion primarily targets minor species, by probability, these collisions will almost always occur with major species in the system. As a result, the summation in Equation 2.4 need only be carried out over the major species in the flame. The values of the local number densities of the major species can be measured by techniques like Raman scattering, or can be obtained from solving chemical kinetics models.

289

290

291

292

293

294

295

#### 2.3.1.1 Absorption Integral Calculation

296

Let us now briefly examine the first term in Equation 2.3 in further detail. Let  $\phi(\nu)$  represent the normalized lineshape of the absorption line being excited, such that  $\int \phi(\nu) d\nu = 1$ . If  $B_{01}$  is the Einstein coefficient for absorption for the line being excited, the term  $B_{01}\phi(\nu)$  represents the spectral absorptivity of the line at  $\nu$ .  $B_{01}$  is usually presented in  $\text{m}^2/\text{Js}$  for LIF applications. Similarly, let  $I_\nu$  be the spectral intensity of the incident radiation, which is the intensity (power per area) of the laser beam per spectral interval. Let  $\psi(\nu)$  be the normalized spectral profile of the laser lineshape, such that  $I_\nu = I\psi(\nu)$  and  $\int \psi(\nu) d\nu = 1$ .  $I_\nu$  is usually given in  $\text{W}/\text{cm}^2/\text{cm}^{-1}$  for ease of use in laser applications.

297

298

299

300

301

302

303

304

305

The product of the spectral absorptivity and the spectral intensity integrated over the spectrum, gives the pumping rate,  $W_{01}$ , as shown in Equation 2.6. The factor  $c$  is the speed of light, which brings the units of  $W_{01}$  to  $\text{s}^{-1}$ .

306

307

308

$$W_{01} = \frac{I}{c} \int \psi(\nu) B_{01} \phi(\nu) d\nu \quad (2.6)$$

### 2.3.1.2 Population Distribution

309

Once again, consider Equation 2.3, this time focusing on the term  $n_0$ , the number density of the marker species in the lower energy state that are available for excitation to the upper state. In reality, this comprises only a small subset of all the available molecules of the marker species in the system.

310

311

312

313

$$n_0 = n f_0 \quad (2.7)$$

In Equation 2.7,  $n$  is the number density of all marker species over all the energy levels, while the fraction,  $f_0$ , represents the proportion of the marker species that populates the lower energy level.

314

315

316

### 2.3.1.3 Solution

317

Substituting Equations 2.6 and 2.7 into 2.3, and noting that the signal produced is actually integrated over a volume,

318

319

$$\Phi = \int_V \frac{n A_{10}}{A_{10} + Q_{10}} \frac{I}{c} f_0 B_{01} \int_{\nu} \psi(\nu) \phi_j(\nu) d\nu dV \quad (2.8)$$

In Equation 2.8, the absorption integral from Equation 2.6 is highlighted in red. The outer integral is performed in space, over the portion of the flame illuminated by the laser sheet. Under the assumption that the laser intensity is uniformly distributed over the sheet thickness, it is possible to rewrite the outer integral as a 1-D integral over the thickness of the flame by replacing the laser intensity,  $I$  with the laser power,  $P$ .

320

321

322

323

324

325

$$\Phi = \frac{P}{c} \int_x \frac{n A_{10}}{A_{10} + Q_{10}} f_0 B_{01} \int_{\nu} \psi(\nu) \phi_j(\nu) d\nu dx \quad (2.9)$$

Equation 2.9 is thus, the solution to the two-level model in the weak excitation

326

limit. Note that the LIF signal varies linearly as the incident laser power (or intensity).  
 Consequently, the weak excitation limit is also referred to as the linear regime.

For the sake of completion, we will briefly mention the other limit of the two-level model solution that occurs when the rate of pumping far exceeds the relaxation rate ( $W_{01} \gg A_{10} + Q_{10}$ ). This is called the saturated limit and in this limit, the fluorescence signal ceases to change with the intensity of the incident laser beam. Operating in this regime is generally not preferred due to several reasons. First, the magnitude of the LIF signal per unit incident laser intensity tends to be the maximum in the linear regime. Once the variation ceases to be linear (even before nearing the saturation limit), we get diminishing returns for increasing the laser power. Further, the saturation criterion (maintaining a high laser intensity) is difficult to satisfy simultaneously in the spatial, temporal and spectral domains. For these reasons, we will restrict our discussion hence forward the linear regime only.

### 2.3.2 CH PLIF Process

In this section, we will examine the limitations of trying to apply the two-level model to describe the CH PLIF process.

Laser-Induced Fluorescence is a multi-step process. First, the marker species absorbs a photon and transitions from a lower energy state to a higher one. This is followed by several physical processes, of which only one pathway leads to the spontaneous de-excitation of the excited molecule, accompanied by the release of a photon. The de-excitation can—but does not need to—take the molecule back to the original state. If the molecule does return to its original state, the fluorescence is said to be resonant. Due to the difficulty of measuring fluorescence signals at the same wavelength as the excitation beam, most practical applications of LIF tend to be non-resonant. The choice of the spectral and temporal properties of the excitation laser source, and of the detected fluorescence emission, constitute the excitation and

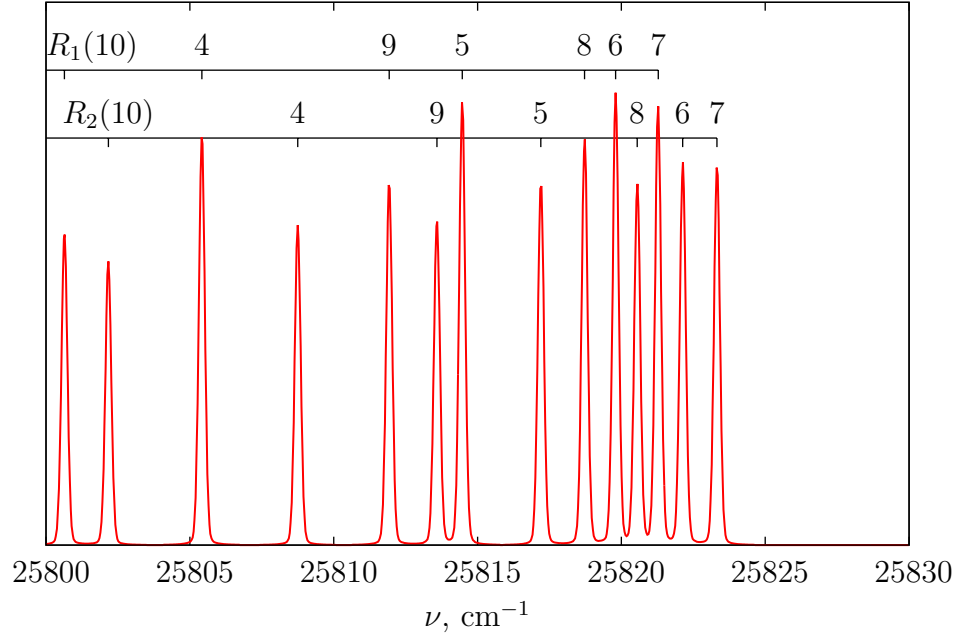


Figure 2.2: The figure shows the frequencies of the absorption lines near the R-bandhead of the CH  $B^2\Sigma^- \leftarrow X^2\Pi$  (0,0) band. The individual lines are labeled with corresponding  $N''$  quantum number.

detection schemes.

The excitation scheme chosen for this study follows the work done by Li et al.[\[12\]](#) who used a ring-cavity, pulsed alexandrite laser to provide excitation in the vicinity of the R-bandhead of the CH  $B^2\Sigma^- \leftarrow X^2\Pi$  (0,0) system. This bandhead, shown in Figure 2.2, is found at a wavelength of about 387.2 nm and represents transitions from a ground state rotational quantum number of  $N'' = 7$ . When operated in multimode, alexandrite lasers have relatively large bandwidths (a few  $\text{cm}^{-1}$  is not uncommon) and hence make it possible to excite several of the neighboring transitions near the bandhead. The current implementation excites CH molecules in the ground state  $X^2\Pi$ ,  $v'' = 0$  with rotational quantum numbers  $N''$  between 5–9.

Upon excitation, these molecules transition to the second electronically excited  $B^2\Sigma^-$  state and populate the lowest vibrational level, ( $v' = 0$ ). Since these transitions occur in the R-branch, the rotational quantum number increases by +1, resulting in the population of the  $N'$  levels between 6–10. At this point, the following possibilities



exist for the excited molecule:

1. The molecule can undergo inelastic collisions with other molecules, resulting in relaxation in the rotational, vibrational or electronic manifolds.
2. The molecule can spontaneously emit a photon and return to any of the lower energy states.
3. The molecule can experience stimulated emission in the presence of another photon of the appropriate frequency and return to any of the lower energy states.
4. The molecule can experience further excitation either by absorbing a photon or through collisional means and can react chemically.

Now, let us examine these potential pathways in greater detail. The first pathway pertains to relaxation. The excitation and subsequent population of a higher energy state causes the CH population distribution to deviate from the equilibrium Boltzmann distribution. The degree of relaxation possible is limited by the lifetime of the energy level the excited species occupy. The collision-free, radiative lifetime of the  $B$  electronic state is about 300 ns[60]—long enough for sufficient rotational relaxation to occur, but too short for complete vibrational relaxation. Based on experiments conducted by Garland et al.[61], it is estimated that the vibrational energy transfer between the two bound states available to the  $B^2\Sigma^-$  state is about two orders of magnitude slower than the rotational energy transfer. As a result, we may suppose that the vibrational manifold remains relatively unaffected, while the rotational manifold is relaxed closer to an equilibrium distribution. The question of the electronic relaxation will be addressed later in this discussion.

The second option available for the excited CH molecule is to spontaneously emit a photon and return to a lower energy state. Spontaneous de-excitation to the ground

state primarily follows the diagonal  $B^2\Sigma^- \rightarrow X^2\Pi$  (0,0) band. The rate of such spontaneous emission between two states is given by the Einstein emission coefficient for the transition. Once again, we will defer discussion of the  $B - A$  transition until later in this discussion.

The third option is for the CH molecule to experience stimulated emission in the presence of a photon of an appropriate frequency. It is highly unlikely that the apposite photon would have a frequency other than the excitation laser. The rate of stimulated emission induced by the excitation laser beam is proportional to the Einstein absorption coefficient for the transition. Other photons that can induce stimulated emission in the CH molecules could originate from spontaneous emission or CH\* chemiluminescence. As mentioned earlier, it is highly unlikely that these will result in stimulated emission of any significant proportion. In part, this is due to the spatial distribution of CH in a typical flame. In Chapter 1, it was stated that CH molecules are expected to be found only in the thin reaction zone of the flame. This causes most photons to be emitted in directions away from the flame, reducing their chance of encountering more CH molecules. Since CH is a minor species, its concentrations are inherently too low, further reducing the likelihood of this pathway.

The fourth option is for the molecule to experience further excitation by absorbing multiple photons or through collisions with other energetic molecules in the system. Since most available photons do not match any transitions from the  $B^2\Sigma^-$ ,  $v = 0$  state, it is unlikely to experience multi-photon excitation. However, collisional removal of CH molecules from the  $B$  state is certainly possible.

Having listed all the options, let us resume the discussion on the possibility of electronic energy transfer from the excited  $B^2\Sigma^-$ ,  $v' = 0$  state. The spacing of the energy levels in the CH system, shown in Figure 2.3, is such that the  $B^2\Sigma^-$ ,  $v' = 0$  state is found to be near-degenerate with the  $A^2\Delta$ ,  $v = 1$  energy level. Consequently, the  $B^2\Sigma^- \leftrightarrow A^2\Delta$  (0,1) transition is reversible. Due to this, collisional population of

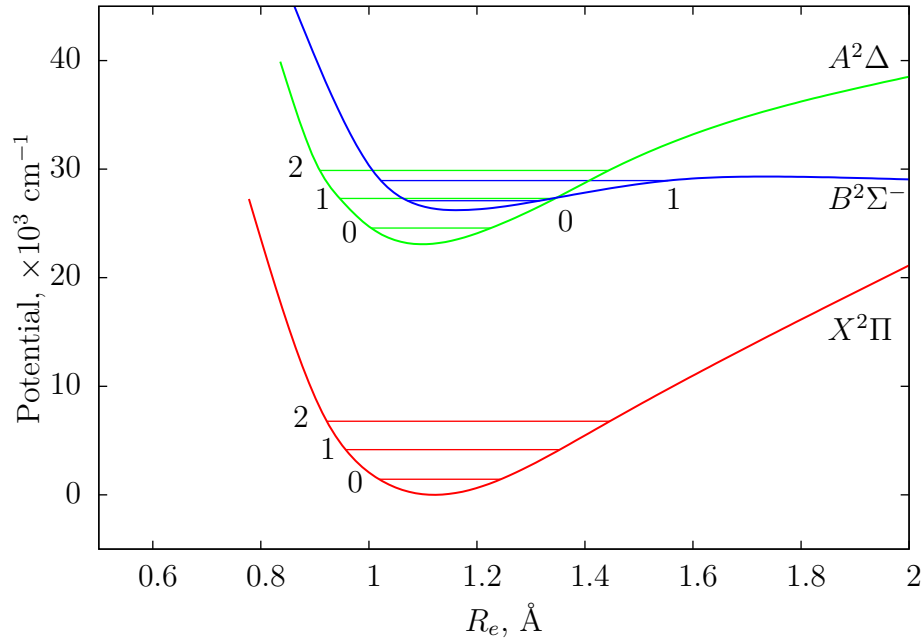


Figure 2.3: The figure shows the RKR potential curves for the  $X^2\Pi$ ,  $A^2\Delta$  and  $B^2\Sigma^-$  energy levels in the CH system. A few vibrational levels are indicated for the  $X^2\Pi$  and  $A^2\Delta$  states. The  $B^2\Sigma^-$  state has only two bound vibrational levels. The diagram is reproduced from Richmond et al.[62] who based it on ab initio calculations by van Dishoeck[63]

the  $A^2\Delta$   $v = 0, 1$  states from the  $B^2\Sigma^-$   $v = 0$  state occurs rapidly. Garland et al.[61] 419  
measured that these transfers account for almost a quarter of all collisional depletion 420  
of the  $B^2\Sigma^-$ ,  $v = 0$  level. Theoretical calculations using overlap integrals between 421  
the involved energy levels predict that a majority of these transfers will be along the 422  
diagonal (0,0) transition.[64]. Instead, experimental data indicates that the number 423  
is closer to a fifth, with almost 80% of the transfers following the near-degenerate 424  
(0,1) pathway. 425

It is this electronic energy transfer mechanism that enables our excitation scheme 426  
to record high quality CH PLIF images. Having now populated the  $A^2\Delta$  states, the 427  
resulting spontaneous emission from the  $A^2\Delta \rightarrow X^2\Pi$  (0,0) and (1,1) transitions can 428  
be easily observed between 420–440 nm. A small portion of the fluorescence in this 429  
wavelength range also occurs from the  $B^2\Sigma^- \rightarrow X^2\Pi$ , (0,1) transition. Since these 430  
emission wavelengths are located far from the excitation wavelength, a simple glass 431

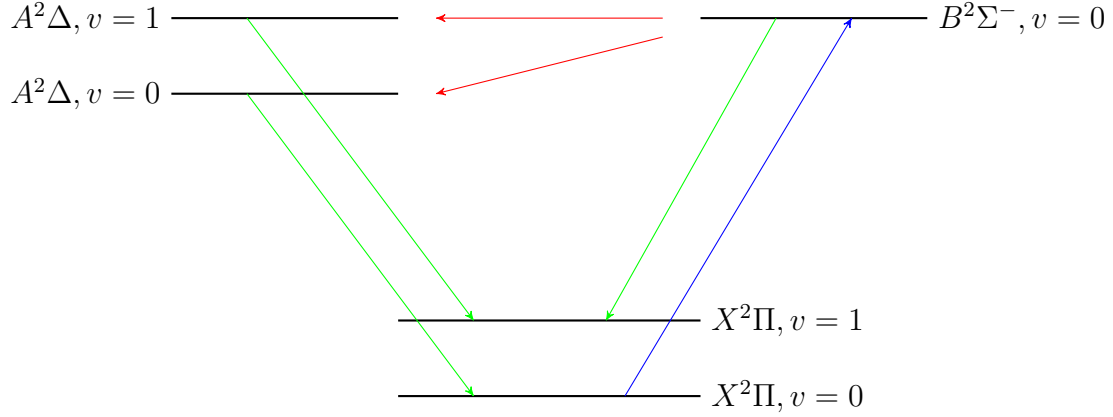


Figure 2.4: Some of the important transitions between energy levels in a CH molecule are shown. The excitation of the CH molecules (blue) is followed by collisional energy transfer processes (red) which populate additional energy levels. Spontaneous emission from some of these energy levels (green) is collected.

filter is sufficient to suppress any elastic scattering from the laser beam.

### 2.3.3 Improved Model

While the two-level model is conceptually simple, applying it to describe the complicated physical process of CH PLIF is challenging. Daily[59] notes, for example, that significant errors can result from using the two-level model to describe even a three-level system. Hence, it is worthwhile to investigate a more complicated model that can describe the CH system with higher fidelity.

Figure 2.4 shows the relevant pathways that lead to the fluorescence emission as discussed in Section 2.3.2. An accurate model of the CH system should involve at least five energy levels, namely the  $B^2\Sigma^-, v = 0$ ,  $A^2\Delta, v = 0, 1$ , and  $X^2\Pi, v = 0, 1$  levels. The model will need to account for collisional transfers between each of these levels, in addition to spontaneous and stimulated transitions. The mathematical solution quickly becomes tedious and complicated. Further, it involves several rate coefficients that have not yet been measured experimentally.

Fortunately, this can be significantly simplified. Previous studies[60, 64] have indicated that the off-diagonal  $B \rightarrow X$  (0,1) transition plays a relatively minor role

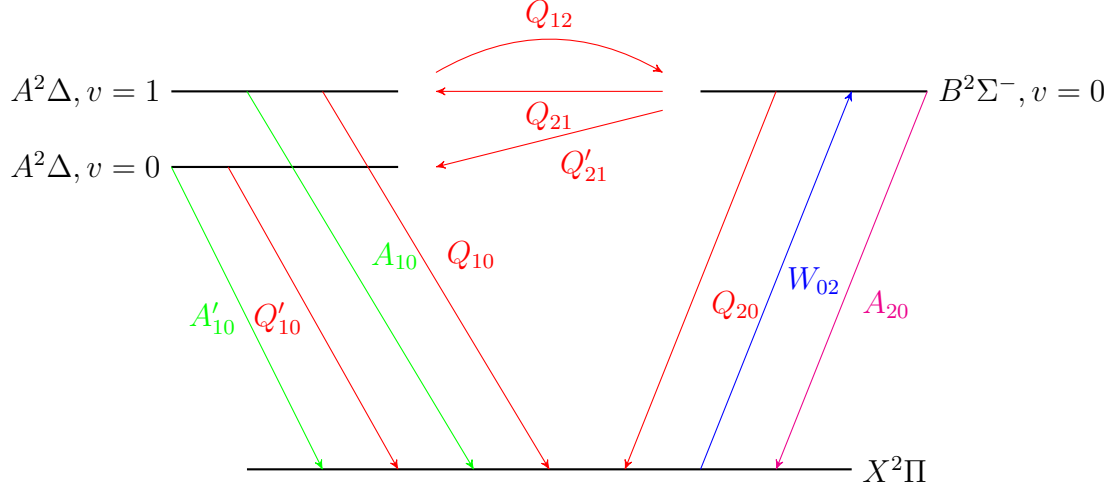


Figure 2.5: A simplified model of the transitions between the energy levels in a CH system. Excitation (blue) of ground state CH molecules to the upper electronic state is followed by several collisional energy transfer processes (red). A small portion of these molecules spontaneously emit a photon (green) and return to ground state. The spontaneous emission corresponding to resonant PLIF (magenta) is not collected.

accounting for only 3.5% of the total fluorescence. Further, the radiative  $A \rightarrow X$  transitions are known[65] to be strongly diagonal, with little or no interaction[61] between the two states. The net result of these two assertions is that we can treat the two  $B \rightarrow A \rightarrow X$  pathways to be disjoint and parallel. The resulting pseudo-three-level model is shown in Figure 2.5.

According to this model, the lower state of the CH system is treated as a single pool that CH molecules are excited from and returned to. This not only neglects the rotational manifold, but also the vibrational manifold of the ground state. This assumption would be valid as long as most of the CH molecules occupy the  $v = 0$  state and the fraction of molecules in the  $v = 1$  state can be safely neglected. At flame temperatures of about 2200 K, this assumption is somewhat questionable as only about 83% of the ground state CH molecules occupy the  $v = 0$  level and as much as 14% are found at the  $v = 1$  state. However, in light of the simplifications afforded to our semi-quantitative model by this assumption, we retain it.

The rates of the various transition processes are indicated in Figure 2.5.  $W_{02}$  is

the pumping process that populates the  $B(0)$  state.  $Q_{ij}$  are collisional energy transfer processes that transfer CH molecules from the  $i$  level to the  $j$  level. The subscripts 0, 1 and 2 represent the electronic energy levels  $X$ ,  $A$  and  $B$ . Processes involving the  $A(0)$  state are differentiated from those involving the  $A(1)$  state by a prime ( $'$ ). Finally,  $A_{ij}$  represents the spontaneous emission coefficients between the  $i$  and  $j$  levels.

Applying Equation 2.1 to this case, we can write an expression for the LIF signal intensity as follows,

$$\Phi = (n_1 A_{10} + n'_1 A'_{10})V \quad (2.10)$$

Our task is to solve for the values of  $n_1$  and  $n'_1$  in terms of  $n_0$ . To do this we need to write rate equations describing the variation of the populations of the three upper states with time.

$$\frac{dn_1}{dt} = -(A_{10} + Q_{10} + Q_{12})n_1 + Q_{21}n_2 \quad (2.11)$$

$$\frac{dn'_1}{dt} = -(A'_{10} + Q'_{10})n'_1 + Q'_{21}n_2 \quad (2.12)$$

$$\frac{dn_2}{dt} = W_{02}n_0 + Q_{12}n_1 - (A_{20} + Q_{20} + Q_{21} + Q'_{21})n_2 \quad (2.13)$$

Under the assumption that the laser excitation time scale is much longer than the collisional time scales, we can set the LHS of Equations 2.11–2.13 to zero. This results in a closed set of linear equations, which can be expressed in matrix form as follows.

$$\begin{bmatrix} A_{10} + Q_{10} + Q_{12} & 0 & -Q_{21} \\ 0 & A'_{10} + Q'_{10} & -Q'_{21} \\ -Q_{12} & 0 & A_{20} + Q_{20} + Q_{21} + Q'_{21} \end{bmatrix} \begin{bmatrix} n_1 \\ n'_1 \\ n_2 \end{bmatrix} = \begin{bmatrix} 0 \\ 0 \\ W_{02}n_0 \end{bmatrix} \quad (2.14)$$

From Equation 2.14, we only need the solutions to  $n_1$  and  $n'_1$ . Substituting the solutions directly into Equation 2.10, we can write the solution in the following form to mirror the expression in Equation 2.3.

$$\Phi = n_0 V W_{02} (Y + Y') \quad (2.15)$$

The terms  $Y$  and  $Y'$  in Equation 2.15 are non-dimensional and represent the fluorescence yields from the two  $A^2\Delta$  states. The functional expression for the yields is more complex now, as shown in Equations 2.16–2.17.

$$Y = \frac{Q_{21} A_{10}}{(A_{10} + Q_{10} + Q_{12})(A_{20} + Q_{20} + Q_{21} + Q'_{21}) - Q_{12} Q_{21}} \quad (2.16)$$

$$Y' = \frac{(A_{10} + Q_{10} + Q_{12}) Q'_{21} A'_{10}}{(A'_{10} + Q'_{10})((A_{10} + Q_{10} + Q_{12})(A_{20} + Q_{20} + Q_{21} + Q'_{21}) - Q_{12} Q_{21})} \quad (2.17)$$

### 2.3.3.1 Absorption Integral Calculation

We now focus on the first portion of Equation 2.15 and consider the rate of population of the upper  $B^2\Sigma^-$  state. As in case of the simple model, this term involves the computation of the integral of the product of the laser linewidth function,  $\psi(\nu)$  and the absorption linewidth function,  $\phi(\nu)$ . However, since our excitation scheme targets multiple lines in the R-bandhead, we actually have a summation of several absorption lines in this integral.

$$\begin{aligned} W_{02} &= \frac{I}{c} \int \psi(\nu) \sum_j B_j \phi_j(\nu) d\nu \\ &= \frac{I}{c} \sum_j B_j \int \psi(\nu) \phi_j(\nu) d\nu \end{aligned} \quad (2.18)$$

In Equation 2.18, the terms  $B_j$  are the absorption coefficients,  $B_{02}$ , for each tran-

sition being excited, each of which has its own broadened linewidth,  $\phi_j(\nu)$  at the local conditions. The discussion of the various sources of line broadening that need to be considered for our case is deferred till Chapter 4.

### 2.3.3.2 Population Distribution

Equation 2.19 presents the expression for  $f_j$  in terms of the vibrational and rotational quantum numbers,  $(v, J)$ , of the energy level  $j$ .

$$f_j(v, J) = \frac{\exp\left(\frac{-hcE_v(v)}{kT}\right)(2J+1)\exp\left(\frac{-hcE_r(v, J)}{kT}\right)}{Q_{rv}} \quad (2.19)$$

The vibrational energy,  $E_v(v)$  of a level is calculated according to Equation 2.20, while the rotational energy,  $E_r(v, J)$  is calculated according to Equation 2.21.

$$E_v(v) = \omega_e \left(v + \frac{1}{2}\right) - \omega_e x_e \left(v + \frac{1}{2}\right)^2 + \omega_e y_e \left(v + \frac{1}{2}\right)^3 - \omega_e z_e \left(v + \frac{1}{2}\right)^4 \quad (2.20)$$

$$E_r(v, J) = \left\{B_e - \alpha_e \left(v + \frac{1}{2}\right)\right\} J(J+1) - \left\{D_e + \beta_e \left(v + \frac{1}{2}\right)\right\} J^2(J+1)^2 \quad (2.21)$$

The  $B^2\Sigma^- \leftarrow X^2\Pi$  transition of the CH system is governed by Hund's Case b and hence, the appropriate rotational quantum number to use is  $N$ . For each rotational quantum number  $N$ , there are two possible values of  $J$  given by  $N \pm \frac{1}{2}$ . The rovibrational partition function,  $Q_{rv}$  is a summation over all available vibrational and rotational levels in the  $X^2\Pi$  state. In practice, this summation over the vibrational states may be truncated at  $v = 4$  and the summation over the rotational states may be truncated at  $N'' = 22$  with negligible loss in accuracy. The values of the various spectroscopic constants in the above equations will be presented in Chapter 4.



### 2.3.3.3 Solution

507

The solution for the rate of production of fluorescence photons can be written in the following form that mirrors Equation 2.9.

508

509

$$\Phi = \frac{P}{c} \int_x n_{CH}(Y + Y') \sum_j f_j B_j \int_\nu \psi(\nu) \phi_j(\nu) d\nu dx \quad (2.22)$$

The expressions for the fluorescence yields,  $Y$  and  $Y'$ , still have many variables that have not been tabulated conveniently in literature. As a result, further simplifications will need to be made on the basis of reported experimental observations. These simplifications are outside the scope of this chapter and will be introduced in Chapter 4 along with the results of applying this model to various reactant mixtures.

510

511

512

513

514

## CHAPTER 3

515

### EXPERIMENTAL METHODS AND CONSIDERATIONS

516

The current chapter describes the experimental apparatus and the diagnostic approaches used in this work. The first section presents a detailed description of the LSB configurations that were tested, along with the testing facilities used for the experimental work. The second section focuses on the selection and implementation of the diagnostic techniques that were used to study flames and flow fields. Further, data reduction techniques used to process the acquired raw data is also described.

#### 3.1 LSB Configurations

523

Two configurations of the Low Swirl Burner were tested for this study. There are referred to in what follows as Configurations A and B. Each configuration consists of the reactant flow inlet, the swirler device, the conduit to the combustion zone and the combustion zone itself. All swirlers tested for this work have an outer diameter,  $d_s$  of 38 mm (1.5 in). Other key dimensions of the swirlers tested are presented in Table 3.1.

Each configuration is housed in a high pressure testing facility. The testing facility consists of an air and fuel supply system, a pressure vessel with adequate optical access and an exhaust system for the products. Each testing facility is instrumented to measure temperatures and pressures which are then used to calculate various flow parameters of interest.

The design of the configurations tested, along with that of their respective test facilities are discussed in greater detail in this section.

Table 3.1: *The dimensions of the swirlers used and the respective perforated plates are presented. Each swirler is referred to by its vane angle (as in “ $S_{37^\circ}$ ”).*

Geometric parameter	Swirlers		
	Configuration A $S_{37^\circ}$	$S_{45^\circ}$	Configuration B $S_{40^\circ}$
<b>Swirler data</b>			
Outer diameter, $d_s$ , mm	38	38	38
Diameter ratio, $\frac{d_i}{d_s}$	0.66	0.66	0.66
Vane angle, $\alpha$	$37^\circ$	$45^\circ$	$40^\circ$
Theoretical Swirl Number, $S$	0.48	0.64	variable
<b>Perforated plate data</b>			N/A
Open area, $\text{mm}^2$	155.97	156.98	-
Blockage, %	71.54	71.36	-
Plate thickness, mm	1.27	1.27	-
Hole pattern	1 - 8 - 16	1 - 8 - 16	-
Hole location (dia), mm	0 - 10.2 - 19.1	0 - 10.2 - 19.1	-
Hole diameter, mm	2.79 - 2.79 - 2.84	2.82 - 2.82 - 2.83	-

### 3.1.1 Configuration A

Preliminary experiments involving velocity field mapping and flame imaging were performed using this configuration. The schematic of the high pressure test facility housing this configuration is shown in Figure 3.1, while the configuration itself is shown in greater detail in Figure 3.2.

#### 3.1.1.1 Test Facility

Pressurized air is supplied from external tanks and heated in an indirect, gas-fired heat exchanger to about 500 K. The flowrate of the air is metered using a sub-critical orifice flow meter with a 38 mm (1.5 in) bore diameter Flow-Lin orifice plate capable of metering a maximum flow rate of 2.2 kg/s (1 lb/s). The orifice flow meter is instrumented with an Omega PX725A-1KGI pressure transmitter calibrated to a reduced pressure range of 0–2.758 MPa (0–400 psi), a shielded K-type thermocouple and an

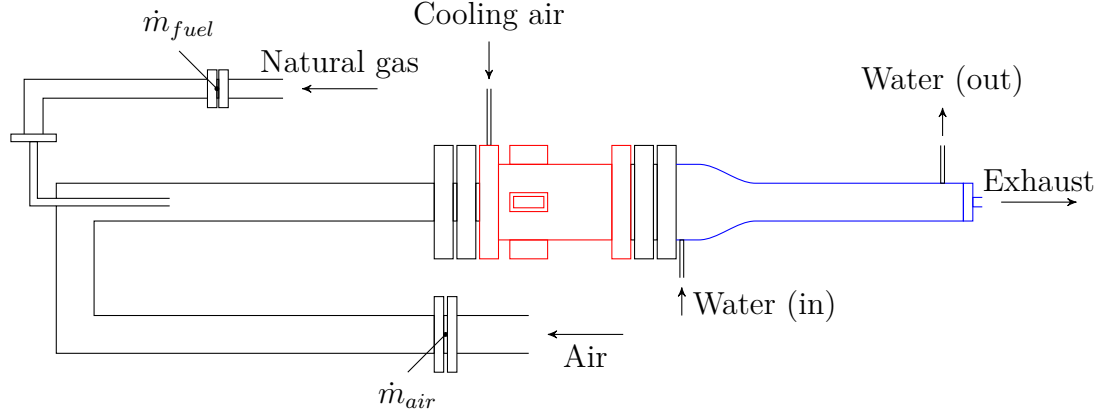


Figure 3.1: A schematic of the high pressure testing facility where Configuration A was operated is shown. The pressure vessel is outlined in red, while the water-cooled exhaust section is outlined in blue. The locations of the orifice flow meters used to measure the mass flow rates of the preheated air and natural gas fuel are indicated.

Omega PX771A-025GI differential pressure transmitter, calibrated to a reduced dif- 549  
ferential pressure range of 0–68.948 kPa (0–10 psid). The fuel (natural gas) is metered 550  
using a similar set up as the air line, with a sub-critical orifice flow meter. The fuel 551  
orifice plate is a Flow-Lin orifice plate with a bore diameter of 13.46 mm (0.53 in), 552  
capable of metering a maximum flow rate of 0.22 kg/s (0.1 lb/s). The upstream pres- 553  
sure is measured using an Omega PX725A-1KGI pressure transmitter (same as the 554  
air line) and the differential pressure is measured using a PX771A-100WDC differ- 555  
ential pressure transmitter with a pressure range of 0–2.489 kPa (100 in H<sub>2</sub>O). The 556  
temperature of the fuel is assumed to be the same as the nominal room temperature 557  
(300 K). 558

The air enters the inlet nozzle of the LSB through a 1.8 m (6 ft) long, 102 mm (4 559  
in) diameter straight pipe section. The fuel flow is choked prior to mixing with the 560  
flow at the head of the straight pipe section. The straight pipe section allows for the 561  
flow to be fully developed, and fully premixed before the reactants enter the burner. 562  
The combustor pressure and temperature are measured at the head of the inlet nozzle. 563  
The pressure is measured by an Omega PX181B-500G5V pressure transducer with a 564  
pressure range of 0–3.45 MPa (0–500 psi), while the temperature is measured using 565

a K-type thermocouple.

The pressure and temperature measurements are used to calculate the four primary flow parameters (combustor pressure, preheat temperature, reference velocity and equivalence ratio) for the LSB in real time. All measurements are monitored and recorded during the course of the experiment by a LabView VI.

The pressure vessel enclosing the combustor is designed to withstand pressures of up to 30 atm and is insulated from the combustor by a ceramic liner. Cooling for the pressure vessel and the quartz tube is provided by a flow of cold air introduced at the head of the pressure vessel. The cold air is drawn from the same external tanks as the main air line, but bypasses the heating system. The cold air flow is not metered, but its upstream pressure is coupled to the main air line so as to ensure a steady flow of cold air into the pressure vessel at all operating conditions. Optical access to the combustor is provided through four 25 mm (1 in) thick, 150 mm (6 in)  $\times$  75 mm (3 in) quartz windows located 90° apart azimuthally. The view ports allow the combustor to be imaged from the dump plane to an axial distance of 150 mm (6 in) downstream.

The exhaust from the combustor is cooled by cold water circulated through a water jacket enclosing each section of the exhaust pipe. The length of the exhaust pipe sections is about 1.8 m (6 ft). The exhaust pipe section terminates in an orifice plug that provides back pressure to the combustion chamber. A different diameter orifice is used for each reference velocity condition tested. The exiting products finally pass through the building exhaust system.

### 3.1.1.2 Low Swirl Burner

The detail of the LSB configuration is shown in Figure 3.2. The premixed, preheated reactants reach the swirler through a converging nozzle that decreases linearly in diameter from the inlet diameter of 102 mm (4 in) to the outer diameter of the swirler, 38 mm (1.5 in). At the swirler, the flow splits into two streams—one passing

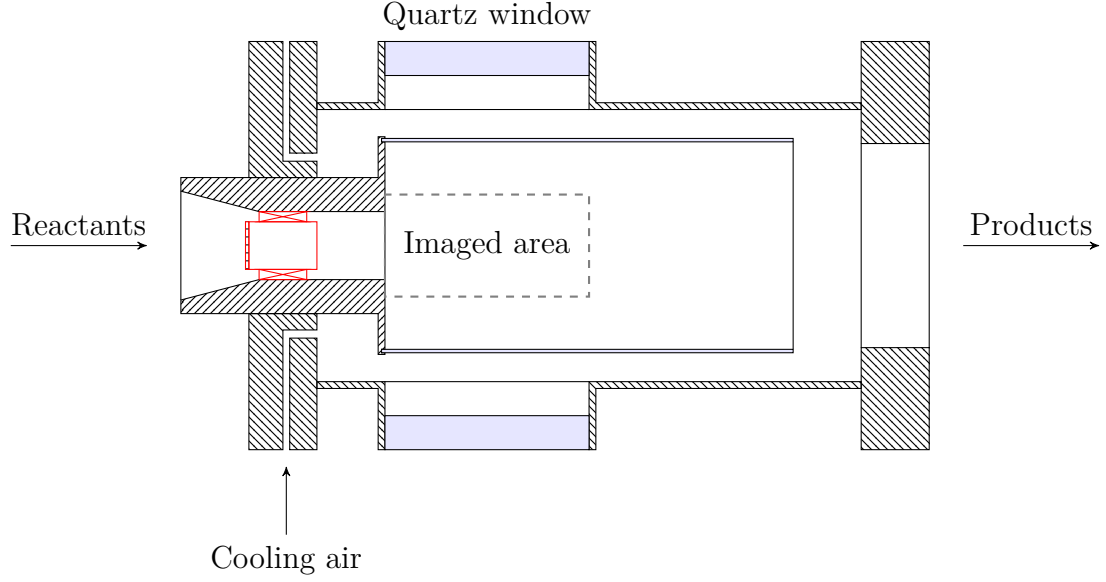


Figure 3.2: A cross-sectional view of Configuration A in the pressure vessel is shown. The reactants enter from the left. The products mix with the cooling air and leave on the right. The location of the swirler in the inlet nozzle is highlighted in red. Also shown is the region of the combustion zone that can be imaged through the quartz windows.

through the central section and another picking up swirl by flowing over the vanes in the annular region. The relative flow split between the two streams is controlled by inducing blockage into the central flow by means of a perforated plate. The swirler leads to a constant area nozzle, and is located one diameter upstream of an abrupt area change. At the area change, the reactants expand from the 38 mm (1.5 in) diameter nozzle into a 115 mm (4.5 in) diameter combustion zone. This expansion ratio is chosen so as to avoid confinement effects on the centerline flame flow field.[27]

The main combustion zone begins at the dump plane and is enclosed by a GE 214 quartz tube. The quartz tube is 300 mm (12 in) long and 115 mm (4.5 in) in diameter. The thickness of the quartz tube is 2.5 mm (0.1 in).

### 3.1.2 Configuration B

This configuration is used to image the flame structure of the LSB flame using CH PLIF. A schematic of the flow system of the test facility is shown in Figure 3.3, while

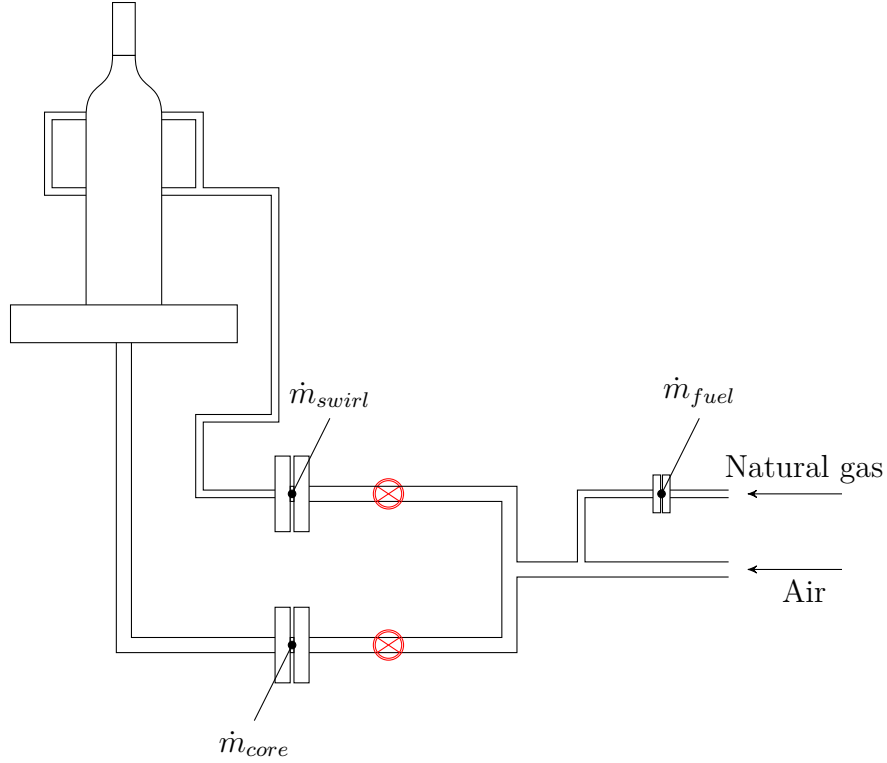


Figure 3.3: A schematic of the high pressure testing facility where Configuration B was operated is shown. The locations of the orifice flow meters on the reactant streams and fuel lines are shown. Valves (shown in red) on the swirl and core flow lines allow for the relative mass flow split to be varied between the two reactant streams. The upstream orifice flow meter on the preheated air line is not shown here. All preheated air lines are insulated.

the LSB combustor itself is shown in greater detail in Figure 3.4.

### 3.1.2.1 Test Facility

This test facility shares the upstream supply of preheated air and natural gas with the one used in Configuration A. The flow rate of the preheated air stream is measured using the same orifice flow meter system used in Configuration A—albeit with a smaller 12.921 mm (0.5087 in) diameter bore Flow-Lin orifice plate. The fuel system pressure is regulated from the building supply pressure to a lower required pressure by an adjustable TESCOM regulator and metered using a critical orifice flow meter. The critical orifice on the fuel line has a bore diameter of 0.8128 mm (0.032 in). The pressure upstream of the critical orifice is measured using an Omegadyne

PX409-1.5KGI pressure transmitter with a range of 0–10.34 MPa (0–1500 psig) and the pressure downstream of the critical orifice is measured using a Dwyer 626 series pressure transmitter with a range of 0–3.45 MPa (0–500 psig). The downstream pressure can be used to verify if the critical orifice is choked during operation. The temperature of the fuel is measured upstream by a K-type thermocouple.

The air system is choked with a 5.41 mm (0.213 in) diameter critical orifice before mixing with the fuel. A short distance after mixing, the reactants are split into two separate streams for the central flow and the swirl flow. The central flow rate is measured using a 9.271 mm (0.365 in) diameter sub-critical orifice, instrumented with a Dwyer 626 series pressure transmitter with a range of 0–4.14 MPa (0–600 psig) for measuring the upstream pressure, a K-type thermocouple for measuring the upstream temperature and an Omega PX771-300WCDI differential pressure transducer with a range of 0–74.65 kPa (0–300 in  $\text{H}_2\text{O}$ ). The swirl flow rate is measured similarly, using a 11.68 mm (0.46 in) diameter sub-critical orifice, a Dwyer 626 series pressure transmitter with a range of 0–5.52 MPa (0–800 psig), a K-type thermocouple and another Omega PX771A-300WCDI with a differential pressure range of 0–74.65 kPa (0–300 in  $\text{H}_2\text{O}$ ). The relative flow split between the two reactant streams is controlled by partially closing gate valves on the two lines. All measurements are monitored and recorded by a LabView VI.

The test rig is designed operated with a pressure vessel and is rated for pressures as high as 30 atm. Unfortunately, due to experimental setbacks, the rig could not be operated at high pressure for the experiments performed in this study. As a result, the combustor was operated without a pressure vessel. The products are vented into the same building exhaust system as Configuration A.



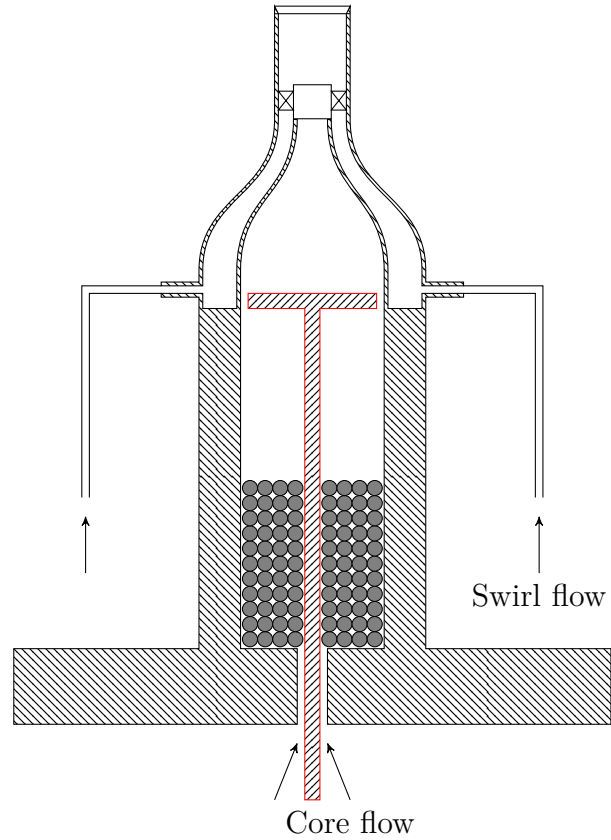


Figure 3.4: A cross-sectional view of Configuration B is shown. The core flow reactants enter through ports in the base flange. Stainless steel ball bearings partially fill the plenum chamber and render the core flow spatially uniform. The turbulence generator is located within the plenum and is outlined in red. The swirl flow reactants enter through separate pipes and are injected into the contoured nozzle through four ports.

### 3.1.2.2 Low Swirl Burner

The design of this LSB configuration is presented in Figure 3.4. As described earlier, the reactants reach the LSB swirler device through two separate streams. The core/central stream passes through a plenum chamber that is filled with steel ball bearings before approaching the swirler through a smoothly contoured nozzle with a high contraction ratio. The annular/swirl stream reaches the swirler directly through a separate contoured nozzle. The contraction ratio is chosen to inhibit the formation of thick boundary layers in the reactant streams. The core stream passes through the central portion of the swirler, while the annular stream picks up swirl by passing through the vanes of the swirler. The swirler lacks a perforated plate covering the central region as the primary function of the plate—regulating the relative mass flow split—is performed by the test facility itself.

The swirler device is located at the beginning of a constant area nozzle which is 57.2 mm (2.25 in) in length. Following this, the reactants expand into the combustion zone.

Unlike Configuration A, there is no dump plane or quartz tube to provide confinement to the combustion zone. The co-flow of cold air provides insulation to the walls of the pressure vessel. Also, as mentioned earlier, the relative mass flow split between the central and annular flows can be controlled directly. Finally, the level of turbulence in the central flow can be adjusted by use of a turbulence generator[66] located upstream in the plenum chamber.

## 3.2 Diagnostics

### 3.2.1 Laser Doppler Velocimetry

The velocity field of the LSB is mapped using a TSI 3-component LDV system. Three wavelengths (514 nm, 488 nm and 476 nm) are separated from the output of a

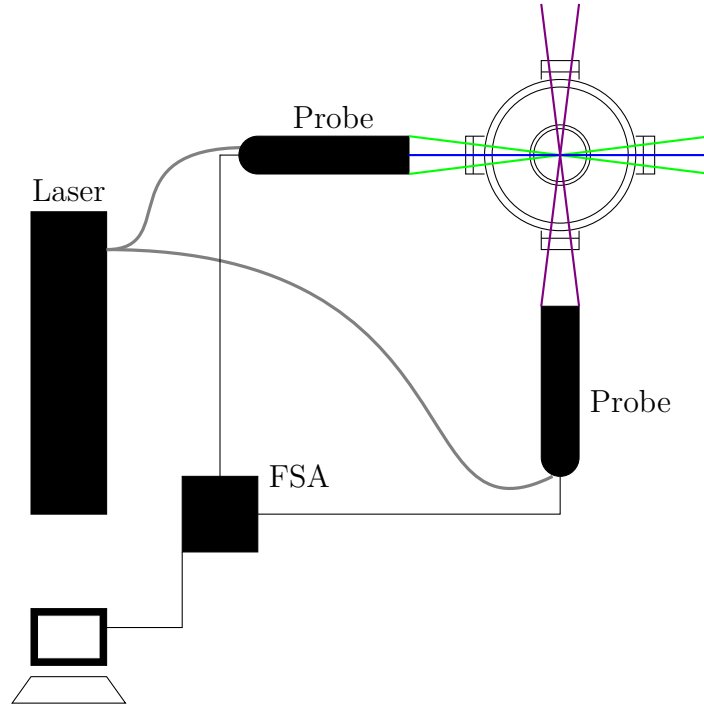


Figure 3.5: The schematic shows the setup employed to map the velocity field of the LSB combustor using Laser Doppler Velocimetry. Three pairs of orthogonal beams are separated from the Argon Ion Laser output and conveyed by fiber optic cables (gray) to optical probes mounted  $90^\circ$  apart about the axis of the LSB combustor. The green, blue, and violet beams in the schematic represent the 514 nm, 488 nm and 476 nm wavelengths. The signal is collected by the transceiver probes and analyzed by the FSA module. The results are saved for further analysis.

5 W Argon ion laser by an FBL-3 multicolor beam generator. The individual beams are split into two coherent beams, which are then focused to intersect and produce interference fringes within an ellipsoidal measurement volume with dimensions of the order of  $100\ \mu\text{m}$ . For this purpose, two transceiver probes are mounted  $90^\circ$  apart about the axis of the LSB. The setup is illustrated in Figure 3.5. One transceiver probe focuses the 514 nm and 488 nm beams in planes perpendicular to each other, while the second probe focuses the 476 nm beams orthogonal to the other two beams. Particles in the flow field crossing the interference fringes scatter the laser light elastically and produce a sinusoidal signal whose frequency is proportional to the velocity of the particle. The transceiver probes collect this scattered light and each wavelength is detected separately by a PDM-1000-3 three-channel photodetector module. The output from the photodetector is processed by an FSA-3500-3 signal processor. The resulting three components of the particle/flow velocity are recorded by the FlowSizer software.

Since the concentration of particulate matter (primarily dust particles) in the airflow is very low, the flow needs to be artificially seeded to facilitate LDV measurements in a reasonable amount of time. The choice of seeding particles to be used and their mean diameter are decided by the characteristics of the flow to be imaged. Since the LSB flow field is a reacting one, the particles need to have high melting points. Further, the particles need to be small enough to follow the flow closely and large enough or reflective enough to scatter light efficiently in the measurement volume. Based on these requirements, commercially available alumina particles with a mean particle diameter of  $5\ \mu\text{m}$  were chosen for this study. In order to uniformly seed the flow, a novel seeding generator was designed as described in Appendix A. The seeding particles were introduced slightly upstream of the 1.8 m (6 ft) long straight pipe section in Test Rig A.

LDV data is only acquired at atmospheric pressure conditions. At high pressure

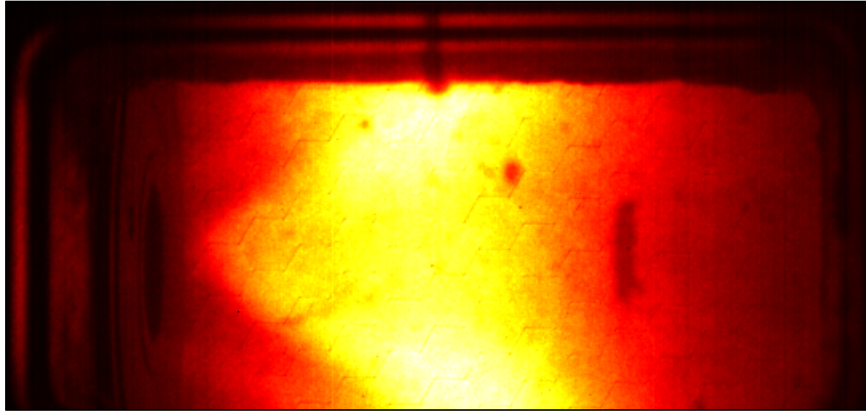
conditions, the reacting LSB flow field produces sharp refractive index gradients that rapidly shift in the turbulent flow field. This causes strong beam steering effects making it very difficult for the laser beams to reliably intersect within such a small measurement volume.[68] The long distance traveled by the beams in the test rig further exacerbate this problem, making LDV data nearly impossible to acquire at such conditions.

### 3.2.2 CH\* Chemiluminescence

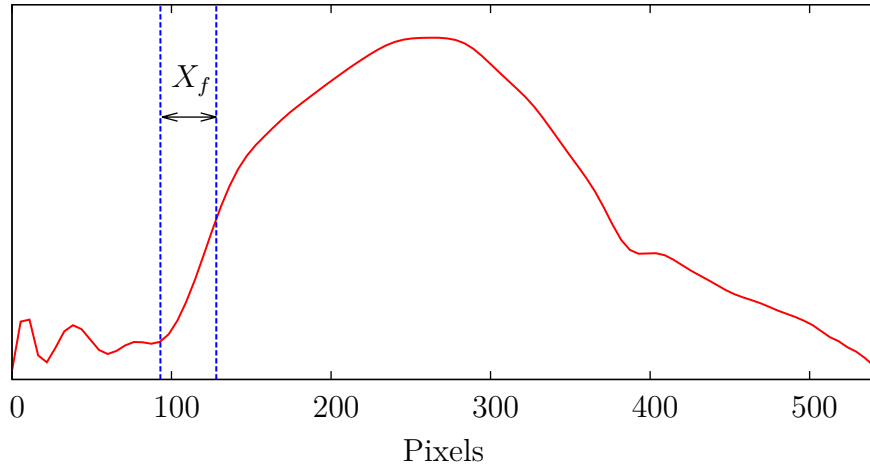
The LSB flame is imaged using one of two 16-bit intensified CCD cameras—PI Acton 1024×256 or 512×512 pixels—with a 28 mm f/2.8 camera lens. The quantum efficiency of the 18 mm Gen III HB filmless intensifier used by the 512×512 camera is about 45% at 430 nm, while the 25 mm Gen II intensifier used by the 1024×256 camera manages about half that at the same wavelength. CH\* chemiluminescence is filtered using a bandpass filter centered on 430 nm with a FWHM of 10 nm. At each operating condition, 100 instantaneous images are acquired with an exposure of 1 ms. An additional 100 instantaneous images are acquired with no flame and averaged to yield the background for correcting the flame images.

#### 3.2.2.1 Image Processing

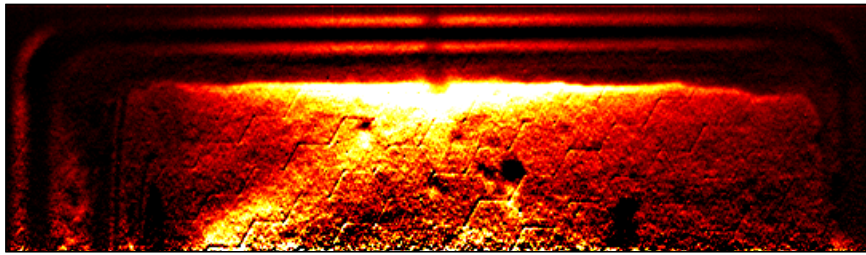
The acquired flame chemiluminescence images are background-corrected and averaged. The resulting mean is the line-of-sight integrated, time-averaged image of the flame. Strictly speaking, this is not the same as a real average obtained from a long exposure image as the instantaneous images are obtained through a periodic sampling process and hence, are prone to statistical errors. However, the behaviour of the flame can be assumed to be sufficiently random that the mean obtained is adequately representative of the true average. Figure 3.6a shows a typical mean CH\* chemiluminescence image prepared in this manner.



(a) Average  $CH^*$  chemiluminescence image



(b) Centerline  $CH^*$  chemiluminescence intensity



(c) Abel deconvoluted half-image

Figure 3.6: These images illustrate the processing of a typical  $CH^*$  chemiluminescence dataset. The top image is the mean of 100 frames and shows the LSB flame at 9 atm. The flame standoff distance is calculated by locating the inflection point in the smoothed intensity profile (middle). An Abel deconvolution (bottom) can be used to highlight the flame brush and measure the angle of the flame.

Even when background-corrected, the walls of the combustor are not at zero intensity in the average chemiluminescence image. This is particularly noticeable near the dump plane where there is no flame present and yet the walls are clearly illuminated. The source of this background illumination is mostly the chemiluminescence from the flame scattering off the combustor and pressure vessel walls. The contribution from blackbody radiation from the heated walls is less significant in the narrow wavelength range imaged. This is evident from images acquired immediately after a flame blowout, which show the walls to be nearly dark even though they should still be hot.

The averaged chemiluminescence image allows us to measure the flame standoff distance by following the intensity profile along the centerline of the combustor. The intensity profile rises sharply when passing the flame standoff location. Thus, the flame standoff location can be ascertained by finding the inflection point in the intensity profile.

The profile of the average chemiluminescence intensity along the centerline of the sample case from Figure 3.6a is shown in Figure 3.6b, showing the flame standoff distance. The distance from the dump plane, measured in number of pixels on the image and scaled by the appropriate magnification factor yields the flame standoff distance,  $X_f$ . The determination of the flame standoff location by this method provides a suitable and deterministic means to locating the leading edge of the flame front.

The average image can be processed further to yield more spatially resolved information about the flame brush. Under the reasonable assumption that the average LSB flame is axially symmetric about the centerline of the combustor, a tomographic deconvolution technique called an Abel deconvolution[69] can be used to convert the line-of-sight integrated image to a radial map of chemiluminescence intensity. In effect, this shows the shape and structure of the average flame brush. The Abel

deconvolution of the sample data from Figure 3.6a is shown in Figure 3.6c.

The Abel-deconvoluted image provides a relatively easy means of determining the flame brush angle. A straight line joining two points located at the center of the flame brush intersects the axis of the combustor at this angle. The angle of the flame is denoted by  $\theta_f$ .

Using the Abel deconvolution to study the flame brush suffers from two main drawbacks. First, the system of equations describing the Abel deconvolution is only valid as long as the entirety of the flame is visible. This is only satisfied in the initial region of the LSB where the diameter of the flame brush is smaller than the height of the optical viewport. At further downstream locations, the flame is not imaged in its entirety. This causes the spurious bright regions near the top of the window in Figure 3.6c. The second limitation of the Abel deconvolution technique stems from the high incidence of errors along the centerline (where  $r \rightarrow 0$ ). Due to this, any study of the flame brush thickness at the flame stabilization point—a metric of considerable importance—is all but impossible using this tomographic technique.

### 3.2.3 CH Planar Laser-Induced Fluorescence

The CH PLIF setup uses the frequency-doubled output of a Light Age PAL 101 alexandrite laser tuned to  $\lambda \approx 387.2$  nm. The design of the laser is shown schematically in Figure 3.7. The active medium is a 150 mm (6 in) long, 5 mm (0.197 in) diameter alexandrite rod. The rod is placed between two flashlamps within the resonator cavity formed by two spherical mirrors. A birefringent tuning element is placed within the resonator to allow the user to select the frequency of the output beam. The tuning element is coupled to a micrometer whose reading relates linearly to the output wavelength. The birefringent filter allows the fundamental wavelength to be varied between 720–780 nm, with peak gain at about 755 nm. The resonator cavity also contains two Q-switches, which allow the laser to optionally operate in



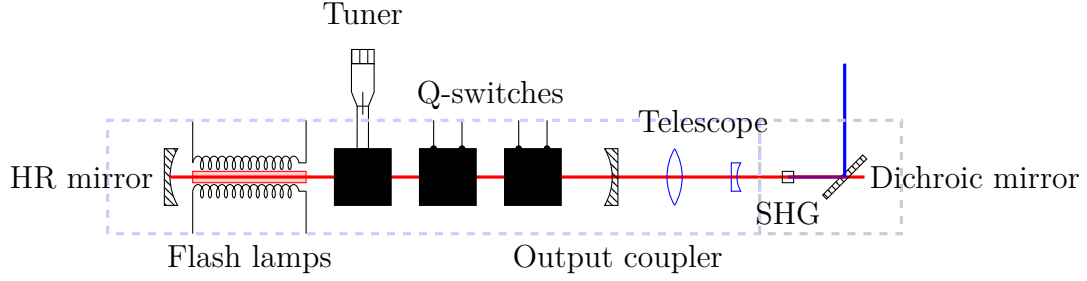


Figure 3.7: A schematic of the components of the PAL 101 Alexandrite laser is shown. The resonator formed by a High Reflection (HR) mirror and an output coupler is built around an alexandrite rod (red) pumped by flashlamps. The frequency of the output is selected by a tuner mechanism. Only one of the two Q-switches was used for this study. The laser beam is reduced in diameter by a collimating telescope (blue) before passing through the Second Harmonic Generator (SHG). The UV beam is separated from the fundamental by a dichroic mirror and exits the laser. The fundamental beam terminates within the laser in a beam dump.

double-pulsed mode. For this study, however, only one Q-switch is used and the laser 769  
is operated in single-pulsed mode only. 770

The diameter of the fundamental beam exiting the output coupler is reduced by a 771  
collimating telescope. This is done in order to increase the efficiency of conversion of 772  
the frequency-doubling crystal. The second harmonic portion of the beam is separated 773  
from the fundamental by a dichroic mirror and exits the laser. The fundamental beam 774  
is terminated at a beam dump within the laser. The exit beam diameter is about 1 775  
mm. 776

The alexandrite laser is capable of operating at frequencies of up to 15 Hz. Laser 777  
power is controlled primarily by varying the voltage applied to the flash lamps. When 778  
operating with a high flash lamp voltage, it is recommended that the frequency of 779  
pulsing be reduced to allow more time to dissipate the heat build up within the 780  
alexandrite rod. All experiments conducted as part of this study operated the laser 781  
at 10.0 Hz. 782

The typical power output of the laser is about 15 mJ/pulse. The pulsewidth of 783  
the laser is about 60-80 ns, as measured by a fast photodiode, and the pulsewidth 784  
decreases with increasing flash lamp voltage. The linewidth of the fundamental beam, 785

as reported by the manufacturer, is 150 GHz at  $\lambda = 775$  nm. Assuming the spectral  
profile of the laser to be a Gaussian, the linewidth of the frequency-doubled beam  
can be determined. The Full Width at Half Max (FWHM) of a Gaussian curve scales  
linearly with the standard deviation of the curve. When convoluted with itself, the  
new standard deviation is  $\sqrt{\sigma^2 + \sigma^2}$  or  $\sqrt{2}$  times that of the original curve. Thus, the  
linewidth of the frequency doubled output is  $150 \times \sqrt{2} = 212$  GHz or  $7.07 \text{ cm}^{-1}$ . In  
wavelength units, this represents a spread of about  $1.06 \text{ \AA}$ .

### 3.2.3.1 Imaging System

All of the PLIF imaging is performed with an intensified PI Acton 512×512 camera.  
The intensified camera is equipped with an 18 mm Gen III HB filmless intensifier  
with a quantum efficiency of about 45% in the 420–440 nm range. The lens is chosen  
depending on imaging requirements of each experiment. In all imaging experiments,  
elastic scattering from the laser beam is attenuated by a 3 mm thick GG 420 Schott  
Glass filter.

### 3.2.3.2 Laminar Flame Setup

Preliminary experiments to evaluate the CH PLIF technique are performed on a  
laminar flame. The choice of a laminar flame as the subject allows us to neglect  
effects of strain and turbulence on the flame. Further, laminar flames are more readily  
simulated by reaction kinetics packages like Chemkin with high fidelity.

These experiments are conducted on a laminar, methane-air flame stabilized on  
an unpiloted Bunsen burner with an inner diameter of 10.16 mm (0.4 in). The air  
flow rate is measured and regulated using a Dwyer rotameter with a range of 0–20  
SCFH calibrated using a Ritter drum-type gas meter. The natural gas flow rate is  
metered using a Matheson FM 1050 602 rotameter with a range from 0–1230 SCCM.  
This flowmeter is calibrated using a Sensidyne Gilibrator 2 bubble flow meter system.

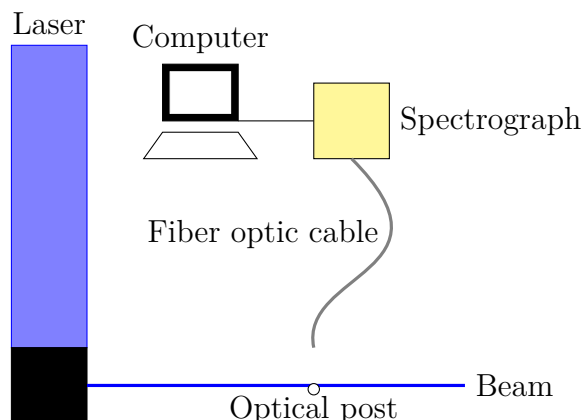


Figure 3.8: The figure above shows the schematic of the experiment performed to calibrate the wavelength of the laser output. The laser output (containing mostly UV, but also a small portion of the fundamental frequency) is glanced off a steel optical post. The scattered light is gathered by a fiber optic cable (gray) and sent to a spectrometer. The spectrum is analyzed to track the location of the fundamental frequency with tuner position. The UV peak is not tracked as the spectrometer is not calibrated for that wavelength.

### 3.2.3.3 Laser Wavelength Calibration

811

As described earlier, the output wavelength of the PAL 101 alexandrite laser is controlled using a micrometer-coupled birefringent tuning mechanism. The wavelength of the laser beam varies linearly with the micrometer reading. Initially, the manufacturer-supplied calibration for the micrometer was found to be inaccurate. This required an experiment to calibrate the laser output wavelength against the micrometer reading in order to determine the slope and offset of the calibration curve accurately.

812  
813  
814  
815  
816  
817  
818

A schematic of this experiment is shown in Figure 3.8. The laser beam is glanced off a steel optical post and the scattered light is collected using a fiber-optic cable coupled to an Ocean Optics HR 2000 spectrometer. The spectrometer is pre-calibrated using 50 wavelengths in the 400–850 nm range from the output of a neon discharge lamp source. The spectrometer is also intensity corrected over this range using a black body source. The estimated error in the resolution of the device is about 0.1 nm (1 Å).

819  
820  
821  
822  
823  
824  
825

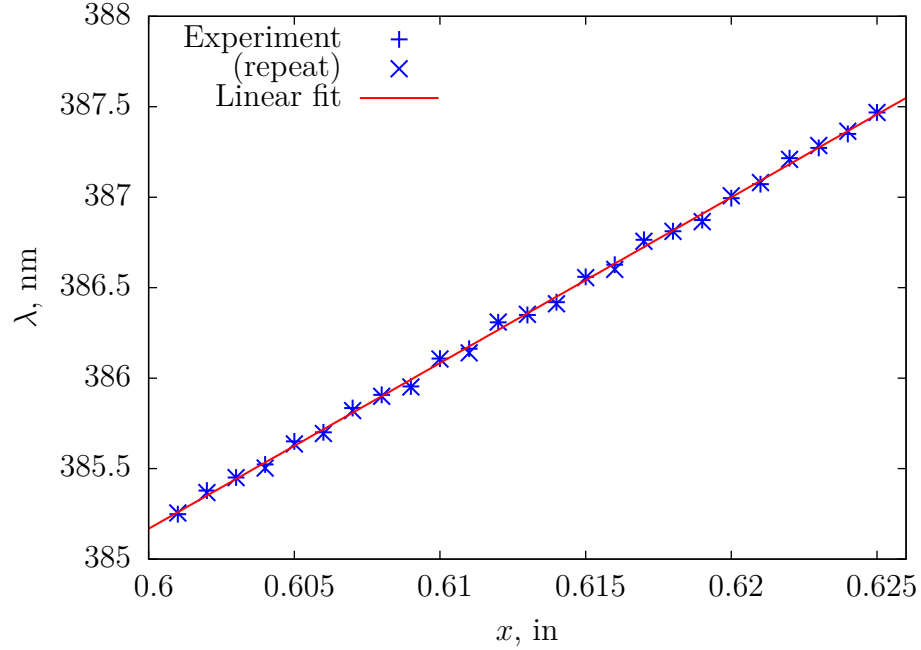


Figure 3.9: The wavelength of the second harmonic beam of the laser is plotted above against the tuner position( $x$ ). The data shows excellent repeatability and falls on a linear trend. The equation for the linear curve fit is  $\lambda = 330.213 + 91.5908x$ , where the units of  $\lambda$  and  $x$  are nm and in, respectively.

The laser micrometer is traversed from 0.600 in to 0.625 in in steps of 0.001 in. 826  
The experiment is repeated by traversing the micrometer from 0.625 in back to 0.600 827  
in along the same points to ensure repeatability and estimate the variation due to 828  
hysteresis. The calibration is performed using at the fundamental wavelength of the 829  
laser as the second harmonic wavelength falls outside the spectrometer's range. Each 830  
spectrum recorded is integrated over 512 ms and averaged over 10 such acquisitions. 831  
The background-corrected peak of the spectrum is then modeled as a Gaussian and 832  
the location of the center of the Gaussian waveform is recorded. 833

The results from this experiment are shown in Figure 3.9. The plot demonstrates 834  
that the variation of the second harmonic wavelength (obtained by halving the fun- 835  
damental wavelength) with the position of the tuner micrometer is linear. Further, 836  
there is little difference between the measurements taken while increasing and de- 837  
creasing the micrometer position. This indicates that any effects of hysteresis in the 838

micrometer position are minimal. The calibration equation relating the micrometer 839  
position to the output wavelength is obtained by applying a linear curve fit to the 840  
data points on the graph as shown in Figure 3.9. 841

## CHAPTER 4

842

### CH PLIF SIGNAL MODELING AND VALIDATION

843

#### 4.1 CH PLIF Preliminary Experiments

844

The CH PLIF imaging system was evaluated for use in imaging hydrocarbon flames by performing two preliminary experiments. First, an excitation scan was performed to confirm the location of the optimal wavelength to excite the CH radicals in a typical hydrocarbon flame. Second, a test of the linearity of the LIF signal with respect to the incident laser intensity was performed. The setup and results of these experiments are described in the following subsections.

850

##### 4.1.1 Excitation Scan

851

An excitation scan is performed by tuning the output of the alexandrite laser from  $\lambda = 387.077$  nm to 387.260 nm. This serves two purposes. First, it locates the optimal wavelength to excite the CH radicals that results in the highest fluorescence yield. Second, the variation of the signal intensity can be compared with simulated profiles from LIFBASE or other spectroscopic calculations and our estimation of the laser linewidth can be validated. The laser linewidth is an integral parameter and appears in the absorption integral used by the models developed in Chapter 2.

852

853

854

855

856

857

858

A schematic of the excitation scan experiment is shown in Figure 4.1. The intensified PI Acton 512×512 camera described in Section 3.2.2 is used to image a premixed, laminar methane-air flame operating at close to stoichiometric conditions. The laminar flame is stabilized on the Bunsen burner described in Section 3.2.3.2. The alexandrite laser is operated at a power of 16 mJ/pulse in the second harmonic. The sheet forming optics consist of a +50 mm cylindrical lens and a +250 mm spher-

859

860

861

862

863

864

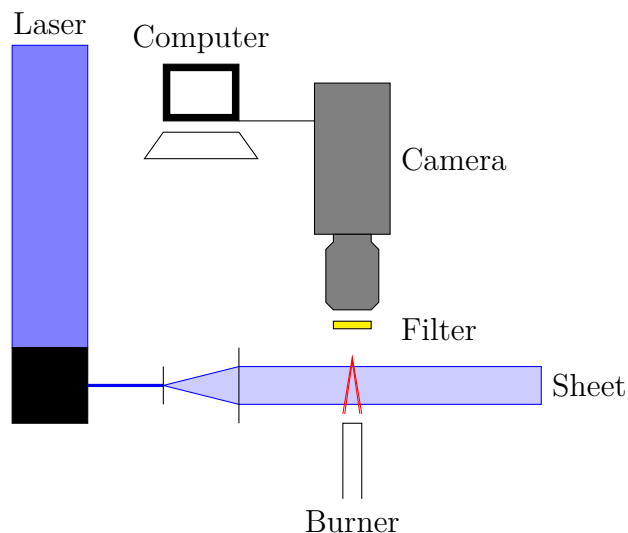


Figure 4.1: The figure above shows the schematic of the excitation scan experiment. A collimating pair of lenses form the laser beam into a sheet focused over a laminar Bunsen burner. The fluorescence is imaged perpendicularly by an intensified camera synchronized to the laser pulse. A 3 mm GG 420 filter is used to reject elastic scattering.

ical lens placed 300 mm apart. The optics form the beam into a collimated sheet 865  
about 25 mm (1 in) tall, focused to a thickness on the order of  $250\ \mu\text{m}$  at the flame 866  
location. The sheet passes through the center of the flame and the edges of the sheet 867  
are blocked by razor blades to prevent reflections from the burner from saturating 868  
the camera. 869

The induced fluorescence in the flame sheet is imaged perpendicularly by the in- 870  
tensified camera using an 85 mm f/1.8 Nikon AF Nikkor lens. A 3 mm thick 50 871  
mm $\times$ 50 mm square GG 420 Schott glass filter is used to reject elastic scattering 872  
at the excitation wavelength. This setup gives a magnification of approximately 62 873  
 $\mu\text{m}/\text{pixel}$ . The camera is triggered by the flash lamp sync signal from the laser sys- 874  
tem and the intensifier is gated over 300 ns, encompassing the 70 ns laser pulse. The 875  
long gate width gives the intensifier enough time to prepare to receive the fluores- 876  
cence, preventing signal loss due to irisng. The gate width is still short enough that 877  
minimal flame chemiluminescence or ambient lighting is recorded in the images. 100 878  
instantaneous images are acquired for each excitation wavelength to acquire a good 879

estimate of the mean fluorescence signal,  $\mu_{sig}$ .

Figure FIXME shows a sample CH PLIF image from this dataset. The images are background-corrected by subtracting the laser scattering (recorded without the flame). The fluorescence signal is calculated from these images using three alternate approaches.

In Method I, two “windows” are identified that include the straight sections of the laminar flame. The average fluorescence signal in each frame is calculated by taking the average of all the emitting pixels in the two windows. A pixel is designated as an emitting pixel if its intensity exceeds the standard deviation of a typical background pixel by at least a factor of five. The average of this value over all the frames is designated as the mean fluorescence signal,  $\mu_{sig}$ . In Method II, the intensity of the pixels is integrated over a straight line connecting the inner and outer edges of the flame. The straight line is chosen along the beam so that the beam intensity does not vary along the integration path. The integration is performed on the left and right arms of the flame, giving two readings per frame. The mean of these values over all the frames is recorded as the mean fluorescence signal,  $\mu_{sig}$ . In Method III, the midpoints of the straight lines from Method II are located and the average of their intensities, over all the frames is recorded as the mean fluorescence signal,  $\mu_{sig}$ . The regions of interest for each of these methods is highlighted in Figure FIXME.

The result of this investigation is shown in Figure FIXME. The calculated mean fluorescence signals from the three methods are plotted against a LIFBASE simulation of the absorption spectrum of the CH  $B-X$  transition. The profiles are appropriately scaled to match the LIFBASE simulation at the maximum value and at the minimum value. The LIFBASE simulation is performed for a thermalized system at 1800 K, at atmospheric pressure. Further, the instrument linewidth is specified to be the same as our estimate of the laser linewidth (1.06 Å).

The profiles of the calculated and scaled mean fluorescence signals are observed to



agree extremely well with the LIFBASE simulation result. The discrepancies between  
the three methods is minimal.

The results indicate that the optimal excitation wavelength, corresponding to the  
highest mean fluorescence signal, is about 387.2 nm. For the rest of the experiments  
performed in this work, the laser is operated at this wavelength. The results also  
help verify that the calibration of the micrometer is accurate and the wavelengths are  
precisely adjustable. Finally, the results validate that our estimated laser linewidth,  
1.06 Å, is accurate. This value can now be used in subsequent calculations of the LIF  
signal levels.

#### 4.1.2 Linearity Test

As explained in Chapter 2, the variation of the fluorescence signal with the excitation  
laser intensity exhibits a saturation curve. For reasons mentioned in that discussion,  
we prefer to operate in the weak excitation limit. Further, the models developed in  
Chapter 2 for calculating the signal are intended to be used in the linear regime.  
Hence, an experiment is performed to verify the linearity of the system response at  
the intensities at which the flames are imaged for this work. The schematic of the  
setup is shown in Figure FIXME. The laser is tuned to the optimal wavelength as  
determined in Section 4.1.1, and operated at 10 Hz. The frequency-doubled beam is  
directed at a steady, laminar, methane-air Bunsen flame operating at a slightly rich  
stoichiometry. The edges of the beam are clipped by an aperture to produce a sharp  
edge and to avoid unnecessary reflections from the burner. No optics are used to  
refract the beam in any way.

The flame is imaged by the PI Acton 512×512 intensified camera equipped with a  
50 mm, f/1.8 AF Nikkor lens. Elastic scattering is attenuated by a 3 mm thick GG 420  
Schott glass filter. The magnification achieved by this set up is about 44 μm/pixel.  
The LIF signal from the flame is recorded in 300 ns gates and accumulated 150 times

before being read out. For each case, a corresponding laser scattering image is also  
recorded for estimating the background. The flame chemiluminescence and ambient  
background are also recorded for the same purpose.

For this experiment, varying the intensity of the laser beam by changing the flash  
lamp voltage or even the Q-switch timing is not preferred as either would alter the  
pulse width of the beam. Instead, quartz disks and blocks of varying thickness are  
introduced into the beam to produce an intensity loss, while preserving all other char-  
acteristics of the beam. The quartz elements decrease the intensity of the laser beam  
through reflection, scattering and absorption. The stray reflections and scattering  
from the quartz elements are contained by enclosing the elements in a box and pre-  
venting these from being recorded by the camera. In this manner, the laser power is  
varied from 10 mJ/pulse to 0.5 mJ/pulse and back.

The acquired images are background-corrected and the intensity is conditionally  
averaged over pixels with a non-zero intensity in the region where the fluorescence  
occurs. The average fluorescence intensity values thus obtained are plotted against  
the corresponding laser intensity and shown in Figure FIXME. A sample image high-  
lighting the region of interest is also shown alongside.

The LIF signal is observed to increase monotonically with increasing laser inten-  
sity. At the lower intensities, the variation is very nearly linear, with marginal scatter  
and only one significant outlier. At intensities above 1 J/cm<sup>2</sup> however, there is sig-  
nificant scatter in the data and the linear trend obtained from the low intensity cases  
cannot be reliably extended over this region.

The results indicate that as long as the intensity of the laser sheet is kept below  
1 J/cm<sup>2</sup>, the assumption of operating in the linear regime is valid.

Table 4.1: *The coefficients of spontaneous emission for transitions in the CH system are provided.*

Transition	Symbol	A, s <sup>-1</sup>
$B \rightarrow X(0, 0)$	$A_{20}$	$2.963 \times 10^6$
$A \rightarrow X(1, 1)$	$A_{10}$	$1.676 \times 10^6$
$A \rightarrow X(0, 0)$	$A'_{10}$	$1.832 \times 10^6$

## 4.2 Fluorescence Signal Modeling

Chapter 2 presented analysis of LIF signal calculation as a function of thermodynamic conditions and the local composition in a flame. Expressions derived using a basic model (Equation 2.9) and a more complex model (Equation 2.22) were presented. The expressions rely on knowledge of several physical values and specific spectroscopic constants pertaining to the CH system.

The basic model requires us to know the Einstein coefficient for spontaneous emission from the “upper” state to the “lower” state. For this, we assume that the “upper” state has the same properties as the  $A^2\Delta$ ,  $v = 0$  state. The improved model, needs the emission coefficients for the  $B^2\Sigma^-$ ,  $v = 0$  and  $A^2\Delta$ ,  $v = 0, 1$  states. These are tabulated from sources in literature[65, 70] FIXME in Table 4.1.

Next, to calculate the fluorescence yield for the basic model, we need to know the quenching cross-sections of major species found in the flames of interest. These cross sections are curve-fitted from several experiments performed over varying ranges of temperature. The functional forms of these cross-sections are presented in Table 4.2.

The fluorescence yield expressions for the complex model require the rates of collisional transfer between several energy levels. There have been efforts to measure and model these rates, but the energy level model used for these studies is more complicated and cannot be easily reconciled with our simplified model. Hence, it would be preferable to make some simplifying assumptions so that the collisional

Table 4.2: *The functional form of the quenching cross-sections of various species with CH are provided.*

Species	$\sigma, \text{\AA}^2$
H <sub>2</sub>	$6.1 \exp(-686/T)$
H	$221T^{-0.5} \exp(-686/T)$
O <sub>2</sub>	$8.61 \times 10^{-6} T^{1.64} \exp(867/T)$
OH	$221T^{-0.5} \exp(-686/T)$
H <sub>2</sub> O	9.6
CH <sub>4</sub>	$52.8T^{-0.5} \exp(-84/T)$
CO	8.31
CO <sub>2</sub>	$8.67 \times 10^{-13} T^{3.8} \exp(854/T)$
C <sub>2</sub> H <sub>6</sub>	13.4
N <sub>2</sub>	$1.53 \times 10^{-4} T^{1.23} \exp(-522.1/T)$
C <sub>3</sub> H <sub>8</sub>	22

rates can be reduced in terms of the quenching rate.

Previous work has reported that the rate of quenching does not appreciably vary over the vibrational manifold, but excited CH molecules in the  $B^2\Sigma^-$  electronic state are approximately 30% more likely to be quenched than molecules in the  $A^2\Delta$  states. This allows us to eliminate  $Q'_{10}$  and  $Q_{20}$  as follows.

$$Q'_{10} = Q_{10} = Q \quad (4.1)$$

$$Q_{20} = 1.3Q \quad (4.2)$$

Our next assumption is based on work by Luque et al.[64] FIXME who reported that the rate of transfer following the  $B^2\Sigma^- \rightarrow A^2\Delta (0,1)$  transition accounts for almost 24% of the collisional removal of CH from the upper electronic state. This allows us to formulate one more equation as shown below.

$$\frac{Q_{21} + Q'_{21} - Q_{12}}{Q_{20} + Q_{21} + Q'_{21} - Q_{12}} = 0.24 \quad (4.3)$$

$$\therefore \frac{R_{21} + R'_{21} - R_{12}}{Q} = 0.4105 \quad (4.4)$$

Next, using the reported results from the same authors[64] FIXME, we know that 986  
the number of CH molecules following the  $B^2\Sigma^- \rightarrow A^2\Delta$  (0,1) transition is four times 987  
as much as the number following the  $B^2\Sigma^- \rightarrow A^2\Delta$  (0,0) transition. 988

$$\frac{Q_{21} - Q_{12}}{Q'_{21}} = 4 \quad (4.5)$$

Finally, Garland et al.[61] FIXME reported that the rate of the forward transfer 989  
along the  $B^2\Sigma^- \rightarrow A^2\Delta$  (0,1) transition is about 60% faster than the reverse process. 990

$$\frac{Q_{21}}{Q_{12}} = 1.6 \quad (4.6)$$

This gives us the third equation forming a closed, linear set of equations in terms 991  
of  $Q_{21}$ ,  $Q_{12}$  and  $Q'_{21}$  that can be written out in matrix form and solved. Equation 4.7 992  
presents the solution. 993

$$\begin{bmatrix} R_{21} \\ R'_{21} \\ R_{12} \end{bmatrix} = \begin{bmatrix} 5.1966 \\ 0.4872 \\ 3.2479 \end{bmatrix} Q \quad (4.7)$$

Substituting Equations 4.1, 4.2 and 4.7 into Equations 2.16–2.17 leads to sim- 994  
plified expressions for the two fluorescence yields. More importantly, they are now 995  
functionally dependent on only the Einstein coefficients and the rate of collisional 996  
quenching. 997

Table 4.3: *FIXME*The coefficients of absorption for selected transitions in the  $CH X(v = 0)$  system are provided.

$N''$	$J_1''$	$\nu_1$ $\text{cm}^{-1}$	$B \times 10^{-9}$ $\text{m}^2 \text{J}^{-1} \text{s}^{-1}$	$J_2''$	$\nu_2$ $\text{cm}^{-1}$	$B \times 10^{-9}$ $\text{m}^2 \text{J}^{-1} \text{s}^{-1}$
1	0.5	25756.08	6.511	1.5	25774.03	5.823
2	1.5	25776.42	7.225	2.5	25782.72	6.489
3	2.5	25792.74	7.532	3.5	25797.06	7.174
4	3.5	25805.42	7.671	4.5	25808.75	7.460
5	4.5	25814.47	7.719	5.5	25817.20	7.581
6	5.5	25819.80	7.708	6.5	25822.13	7.610
7	6.5	25821.28	7.652	7.5	25823.32	7.581
8	7.5	25818.72	7.561	8.5	25820.55	7.506
9	8.5	25811.93	7.439	9.5	25813.59	7.396
10	9.5	25800.64	7.288	10.5	25802.17	7.254
11	10.5	25784.57	7.111	11.5	25785.98	7.083
12	11.5	25763.38	6.907	12.5	25764.70	6.884
13	12.5	25736.65	6.676	13.5	25737.88	6.657
14	13.5	25703.90	6.418	14.5	25705.06	6.402
15	14.5	25664.54	6.129	15.5	25665.64	6.116
16	15.5	25617.87	5.815	16.5	25618.92	5.804
17	16.5	25563.03	5.472	17.5	25564.03	5.463
18	17.5	25499.00	5.101	18.5	25499.95	5.094
19	18.5	25424.52	4.624	19.5	25425.42	4.618
20	19.5	25338.08	4.161	20.5	25338.93	4.156
21	20.5	25237.84	3.674	21.5	25238.64	3.670
22	21.5	25121.60	3.183	22.5	25122.36	3.180

$$Y_1 = \frac{5.1966Q}{(A_{10} + 4.2479Q)(A_{20} + 6.9838Q) - 16.8780Q} \quad (4.8)$$

$$Y_1' = \frac{0.4872Q(A_{10} + 4.2479Q)}{(A_{10}' + Q)((A_{10} + 4.2479Q)(A_{20} + 6.9838Q) - 16.8780Q)} \quad (4.9)$$

The calculation of the quenching rate also requires us to know the number density of the major species in the flame zone. The profile of the local mole fractions of various species through a 1-D, freely propagating, laminar flame was obtained from CHEMKIN solutions using the Flame-Speed Calculator reactor model. Results are

presented in this chapter for laminar flames using a variety of reactant mixtures and inlet conditions. Additional results for strained laminar methane-air flames are calculated using the Opposed flow flame reactor model.

The CHEMKIN results provide mole fractions, which can be used to solve for the number density of each species using the following equation.

$$n_i = \frac{pN_A X_i}{RT} \quad (4.10)$$

In Equation 4.10,  $N_A$  is Avogadro's number,  $X_i$  is the mole fraction of species  $i$ ,  $R$  is the universal gas constant and  $p$ ,  $T$  are the local pressure and temperature in the flame.

Next, in order to calculate the absorption integral, we require the Einstein B-coefficients, along with the line positions of the transitions excited by the laser. These are taken from FIXME and tabulated in Table 4.3. Using these values, it is possible to calculate the optimal laser wavelength that results in the highest value of the absorption integral. The optimal laser wavelength is not a constant value and depends on the temperature and pressure at which the CH molecules are present. Using a typical value of 1800 K for the temperature in the flame zone, the variation of the optimal laser wavelength can be plotted against combustor pressure. As the combustor pressure increases, the absorption lines in the CH  $B^2\Sigma^- \leftarrow X^2\Pi$  (0,0) R-bandhead are increasingly broadened by collisional broadening. Absorption lines that are at slightly lower frequencies, but close to the bandhead can now begin to absorb the laser energy. This causes the optimal laser wavelength to move slightly towards smaller wavenumbers. Figure FIXME shows this variation.

During experiments, this shift contributes negligibly towards increasing the LIF signal and hence, the laser tuner can be left at the optimal location for atmospheric pressure cases.

Returning back to Equations 2.9 and 2.22, we need spectroscopic constants of the

Table 4.4: *Spectroscopic constants for the CH X<sup>2</sup>Π level are presented.*

Constant	Value, cm <sup>-1</sup>
$\omega_e$	2860.7508
$\omega_e x_e$	64.4387
$\omega_e y_e$	0.36345
$\omega_e z_e$	$-1.5378 \times 10^{-2}$
$B_e$	14.459883
$\alpha_e$	0.536541
$D_e$	$1.47436 \times 10^{-3}$
$\beta_e$	$-2.530 \times 10^{-5}$

X<sup>2</sup>Π,  $v = 0$  energy level in order to calculate the Boltzmann fractions,  $f_j$ . These constants have been determined by Zachwieja et al.[71] and are tabulated in Table 4.4.

Next, FIXME, we discuss broadening mechanisms and the analytical expression for the absorption integral.

Consider now, each term in the above integral. The laser lineshape function,  $\psi(\nu)$ , can be modeled as a Gaussian profile without any loss of generality. The linewidth of the alexandrite laser, when operated in broadband mode, is of the order of a few wavenumbers. The effect of line broadening mechanisms, such as natural broadening, inhomogeneous broadening, etc that are commonly encountered in solid state lasers are negligible in comparison and hence, do not affect the lineshape appreciably.

$$\psi(\nu) = \frac{1}{\sigma_l \sqrt{2\pi}} \exp\left(-\frac{(\nu - \nu_l)^2}{2\sigma_l^2}\right) \quad (4.11)$$

The mean of the lineshape profile,  $\nu_l$ , is set by tuning the center wavelength of the laser. The Full Width at Half Max (FWHM) of the laser,  $\Delta\nu_l$ , is prescribed by the manufacturer and can be used to calculate the standard deviation of the Gaussian as



follows.

1041

$$\sigma_l = \frac{\Delta\nu_l}{2\sqrt{2\ln 2}} \quad (4.12)$$

The lineshape of the absorption line being excited, on the other hand, is primarily dictated by mechanisms associated with gas-phase media—collisional broadening and Doppler broadening being the most important ones. Collisional broadening is a homogeneous mechanism and produces a Lorentzian broadened lineshape. The FWHM of the Lorentzian profile is related to the thermodynamic conditions by the following empirical formula.

1042  
1043  
1044  
1045  
1046  
1047

$$\Delta\nu_c = 0.1 \left( \frac{p}{p_0} \right) \left( \frac{T_0}{T} \right)^{0.6} \quad (4.13)$$

In Equation 4.13,  $p_0$  and  $T_0$  represent standard conditions of pressure and temperature (101325 Pa and 300 K) respectively. By contrast, Doppler broadening is an inhomogeneous mechanism that results in a Gaussian lineshape. Its effect depends on the frequency (wavenumber) of the line being broadened,  $\nu_a$ , and on the molecule's velocity. The FWHM of the resulting broadened lineshape is given by,

1048  
1049  
1050  
1051  
1052

$$\Delta\nu_d = \nu_a \frac{\sqrt{\ln 2}}{c} \sqrt{\frac{8kT}{m_{CH}}} \quad (4.14)$$

The combined effect of these two broadening mechanisms can be calculated by convoluting the two broadened lineshapes. FIXME: Note that this assumption is fine if the dominant broadening mechanism is Doppler broadening. However, in combustion systems, particularly at pressure, the dominant mechanism is collisional broadening, making the curve much closer to a Lorentzian shape. In this case, a Lorentzian convoluted with a Gaussian results in a Voigt profile. Lorentzian profiles have more area in the “wings” of the curve than Gaussian profiles. However, since the maximum broadening of the absorption lines is smaller than the linewidth of the laser beam,

1053  
1054  
1055  
1056  
1057  
1058  
1059  
1060

this should not affect our results too much. FIXME: Perhaps a test using a Voigt profile vs a Gaussian profile to model absorption?

In order to simplify the calculations, we assume that the collision-broadened Lorentzian profile is reasonably approximated by a Gaussian profile with the same FWHM. Now, the convolution of the two profiles results in another Gaussian, with the same mean and a FWHM given by,

$$\Delta\nu_a = \sqrt{\Delta\nu_c^2 + \Delta\nu_d^2} \quad (4.15)$$

Thus, the Gaussian lineshape of the broadened absorption line can be written as,

$$\phi(\nu) = \frac{1}{\sigma_a \sqrt{2\pi}} \exp\left(-\frac{(\nu - \nu_a)^2}{2\sigma_a^2}\right) \quad (4.16)$$

In Equation 4.16,  $\nu_a$  is the frequency (wavenumber) of the absorption peak being excited. The standard deviation of the lineshape,  $\sigma_a$ , is related to the broadened FWHM,  $\Delta\nu_a$ , by the following equation.

$$\sigma_a = \frac{\Delta\nu_a}{2\sqrt{2\ln 2}} \quad (4.17)$$

With the above information, the integral in Equation 2.18 can be solved analytically as follows.

$$\int \psi(\nu)\phi(\nu)d\nu = \frac{1}{\sqrt{2\pi(\sigma_a^2 + \sigma_l^2)}} \exp\left(-\frac{(\nu_l - \nu_a)^2}{2(\sigma_a^2 + \sigma_l^2)}\right) \quad (4.18)$$

This formulation of the signal intensity implicitly makes the following assumptions.

1. The fluorescence emission is predicted at steady state.
2. The collection volume is optically thin and an emitted photon is not reabsorbed within the flame itself. This is a reasonable assumption to make, since the flame thickness and the thickness of the laser sheet are both typically quite small.

## 4.3 Results

1078

Comparison of CH concentration predicted by GRI Mech and San Diego mechanisms 1079  
for methane. 1080

## CHAPTER 5

1081

### LSB FLAME CHARACTERISTICS

1082

In Chapter 2, we introduced the salient features of the Low Swirl Burner (LSB) flow field and discussed the mechanisms by which the LSB flame is stabilized. Further, various characteristics of the LSB flame that can be measured from flame images were outlined. To recapitulate, these are the flame location, flame shape and the flame structure. The first two are quantified by the flame standoff distance,  $X_f$ , and the flame angle,  $\theta_f$ , respectively.

1083  
1084  
1085  
1086  
1087  
1088

In the same chapter, we introduced the four flow parameters that describe an operating condition for the LSB — the combustor pressure,  $p$ , the preheat temperature,  $T$ , the mass-averaged inlet velocity (also called the reference velocity,  $U_0$ ), and the equivalence ratio of the premixed reactants,  $\phi$ . We further introduced a geometric parameter — the angle of the vanes of the swirler,  $\alpha$ , which affects the amount of swirl present in the flow field.

1089

1090

1091

1092

1093

1094

The LSB flame was studied over a range of operating conditions, and the effect of flow and geometric parameters on the reacting flow field were investigated. The results of these investigations are presented in this chapter.

1095

1096

1097

#### 5.1 Effect of Reference Velocity

1098

In typical gas turbine applications, varying the loading on the engine does not affect the reference velocity. However, since the reference velocity is a design parameter, the effect it has on the flame characteristics has implications for the design of future LSB-based gas turbine engines.

1099

1100

1101

1102

One of the key objectives of this thesis is to investigate how the LSB flame stabi-

1103

lization operates at high pressure conditions. The simple model described in Chapter 2 predicts a self-similar flow field for the LSB at all reference velocities. This implies that the reference velocity will have no discernible impact on the flame standoff distance. This result is desirable for gas turbine designers, since the flame location and shape can be assumed to be constant. Limited testing conducted in published works confirmed this behavior at atmospheric pressure conditions with no preheat.

In order to verify the validity of this model at high pressure conditions in the presence of substantial preheat, the LSB was operated at a pressure of 6 atm over a range of reference velocities from 10 m/s to 40 m/s. For these tests, the  $S_{37^\circ}$  swirler was used. In a parallel series of tests, the  $S_{45^\circ}$  swirler was tested at a pressure of 3 atm at a reference velocities of 40 and 80 m/s. The location of the flame was measured from CH\* chemiluminescence images, and the results are presented in Figure FIXME.

There is essentially no systematic variation in the flame standoff distance or the flame angle for the low velocity,  $S_{37^\circ}$  tests. Based on the model, this can be interpreted as the increase in reference velocity producing a concomitant increase in the turbulent flame speed at the flame stabilization location, negating any change in the flame's location. In other words, the flow field appears to retain its self-similarity, even at elevated pressures and temperatures.

When the  $S_{45^\circ}$  swirler was tested at higher reference velocities, however, the flame location shifted downstream sharply. This indicates potential limitations to the simple flame stabilization model that may not predict the behavior of the LSB flame at elevated pressures and temperatures, particularly at high reference velocities.

A possible cause of this limitation can be explored by considering the effect of increased reference velocity on the turbulent combustion regime in which the LSB combustor operates. Previous studies have primarily operated the LSB in the flamelet regime where the modified Damköhler model predicts the behavior of the turbulent flame speed with reasonable fidelity. At elevated pressures, both the laminar flame

speed of the reactants,  $S_L$  and the flame thickness,  $\delta_f$  are diminished. This places the operating regime higher and more to the right on a Borghi diagram, as shown in Figure FIXME. While increasing the reference velocity did not affect the turbulent combustion regime at lower pressures in a flamelet combustion regime, at elevated pressures the flame may be transitioning into the thin reaction zone regime. This transition would cause a reduction in  $S_T/S_L$ , or at least a lesser increase, and the turbulent flame speed would no longer be expected to increase in step with  $U_0$  and the increased levels of turbulence. This would explain the the observed downstream shift of the high pressure LSB flame at high reference velocities.

## 5.2 Effect of Preheat Temperature

The preheat temperature of the reactants is a key flow parameter, especially for gas turbine combustors. In general, the rates of most chemical reactions in the flame zone are highly sensitive to the temperature of the reactants. For the LSB in particular, the temperature of the incoming flow directly affects its viscosity and consequently, the velocity field in the flame stabilization region. Thus, studying the effect of the preheat temperature on the LSB flame and flow field is important.

In order to explore this in greater detail, the velocity field of the combustor was mapped using Laser Doppler Velocimetry (LDV). The conditions were chosen to study the effect of increasing the preheat temperature on both reacting and non-reacting LSB flow fields. Further, the study includes both low and high reference velocity cases. The relevant flow parameters relating to these tests are presented in Table FIXME. All LDV tests were limited to atmospheric pressure conditions. Implementing the LDV technique at elevated pressures proved difficult due to beam steering issues, coupled with impractical turn-around times between the successive runs that would be required to obtain sufficient LDV data points for analysis.

The normalized centerline mean and rms axial velocity profiles for the three cases

are presented in Figure FIXME. The abscissa represents the distance from a point 1157  
called the virtual origin,  $X_0$ . The virtual origin is defined as the imaginary location 1158  
where the extrapolated linear axial velocity profile reaches the reference velocity in 1159  
magnitude. The extrapolation is indicated in Figure FIXME by a dashed line. 1160

As noted in Chapter 2, previous studies[33] reported that mean axial stretch 1161  
— the normalized slope of the linear decay of axial velocity — at the inlet of the 1162  
combustor was self-similar, regardless of the Reynolds number,  $Re$  of the operating 1163  
condition. Further, it was reported that the velocity decay was steeper for reacting 1164  
cases compared to non-reacting cases. 1165

The results presented in Figure FIXME however, show that even though Cases 1 1166  
and 2 have similar  $Re$ , their mean velocity profiles have very different slopes. Further, 1167  
the reacting and non-reacting cases (both at preheated conditions) have similarly 1168  
steep slopes. This indicates that the mean axial stretch in the near field of the LSB 1169  
flow field is a stronger function of the preheat temperature than  $Re$ . The presence 1170  
of preheat results in increased viscosity that enhances the momentum transport in 1171  
the radial direction. This causes the velocity decay to be steep for preheated cases, 1172  
compared to cases without preheat. 1173

Assuming that  $S_T$  is constant, these results suggest that at higher preheat tem- 1174  
peratures, the flame would stabilize closer to the dump plane because of the faster 1175  
velocity decay and reduced local flow velocities. In fact, a faster velocity decay would 1176  
produce greater  $u'$  values and increase  $S_T$ , further causing the flame location to shift 1177  
upstream. Furthermore, in view of the steep velocity profile, it may be anticipated 1178  
that any changes in the stabilization location caused by perturbations in the local 1179  
flow field (and hence, the local turbulent flame propagation velocity) are likely to be 1180  
of diminished magnitude in the presence of preheat. All of this leads to an intuitive 1181  
result — the LSB flame behaves more stably at high preheat conditions. 1182

### 5.3 Effect of Swirler Vane Angle

1183

As described in Chapter 3, the LSB swirlers tested for this study are designed to have 1184  
the same mass flow splits. The  $S_{45^\circ}$  swirler has a higher vane angle, resulting in greater 1185  
blockage to the flow passing through the annular section. In order to compensate for 1186  
this, the perforated plate covering the central section has slightly smaller holes. The 1187  
net effect retains the same mass flow split as in the  $S_{37^\circ}$  swirler. 1188

Chapter 2 describes how the swirler vane angle relates to the amount of swirl im- 1189  
parted to the incoming flow. According to Equation FIXME, a swirler with a higher 1190  
vane angle will produce greater swirl in the reactants. Previous work in swirl com- 1191  
bustion[18, 72] has pointed out that increased swirl shortens the flame by enhancing 1192  
the swirl-induced radial pressure gradients. The data acquired in the present investi- 1193  
gation is in agreement with this observation. Operated at identical inlet conditions, 1194  
the  $S_{45^\circ}$  swirler stabilizes a flame closer to the dump plane and with a larger flame 1195  
angle compared to the  $S_{37^\circ}$  swirler. 1196

This result highlights an interesting trade-off for the designers of LSB-based gas 1197  
turbine engines. The  $S_{45^\circ}$  flame is located further upstream and has a more concen- 1198  
trated region of heat release. This enhances the strength of the toroidal recirculation 1199  
zone near the dump plane, which may be powerful enough under certain conditions 1200  
(as we shall see in Section 5.4) to even cause the flame to attach itself to the lip of 1201  
the inlet. All of this means that the  $S_{45^\circ}$  flame is more stable and will resist pertur- 1202  
bations in the incoming flow better than the  $S_{37^\circ}$  flame. However, the presence of 1203  
a strong recirculation zone in the flow field of the  $S_{45^\circ}$  swirler will entrain more hot 1204  
products and retain them longer near the zone of heat release. This is a recipe for 1205  
the production of thermal  $\text{NO}_x$ . While no emission measurements were made as part 1206  
of this study, it may be reasonably anticipated that the  $\text{NO}_x$  performance of the  $S_{45^\circ}$  1207  
swirler will be degraded compared to the  $S_{37^\circ}$  swirler. The trade-off for gas turbine 1208



engine designers is thus between flame stability and emissions performance.

## 5.4 Effect of Equivalence Ratio

The LSB is primarily intended for fuel-lean operation in order to utilize its low  $\text{NO}_x$  emission performance. As a result, most of the testing was done as close as possible to a target  $\phi$  of 0.56. Limited testing was carried out at 12 atm for two off-target conditions: a slightly richer ( $\phi \approx 0.58$ ) and a slightly leaner ( $\phi \approx 0.53$ ) mixture, in order to explore the sensitivity of the LSB flame to limited changes in equivalence ratio. The  $S_{45^\circ}$  swirler was used for these tests. The corresponding averaged and Abel-deconvoluted flame images are presented in Figure FIXME.

Two characteristics of the flame are immediately obvious from these images. First, the zone of heat release, marked by the region from which  $\text{CH}^*$  chemiluminescence is observed, is increasingly compact at fuel-rich conditions. Virtually all other flame images acquired at a leaner condition show a long flame, with the heat release distributed over the entire visible area of the combustor. The compactness of the heat release zone indicates potentially poor  $\text{NO}_x$  performance at these conditions.

Second, the fuel-rich flame brush can be observed to wrap around and anchor itself on the dump plane. This is particularly observable in the Abel-deconvoluted image. The attached region is not as bright as the rest of the flame brush, indicating that the flame may be attaching itself intermittently. This intermittent behavior can be confirmed from the instantaneous images where it is visible on some of the acquired images, but not others. This behavior was alluded to in Section 5.3 as being the result of the enhanced toroidal recirculation zone produced by this swirler. Thus, the intermittent attachment of the flame to the inlet indicates the increased importance of the toroidal recirculation zone in stabilizing the flame.

It should be noted that the reliance on a toroidal recirculation zone to anchor the flame to the inlet is one of the primary flame stabilization mechanisms used by

traditional swirl combustors. Thus, LSB swirlers with high vane angles tend to behave  
like traditional swirl combustors at fuel-rich conditions.

## 5.5 Effect of Combustor Pressure

In many gas turbine engines, the combustor pressure varies directly with the loading  
of the engine. Like the preheat temperature, the combustor pressure affects the LSB  
flame both through the fluid mechanics of the flow and the kinetics of the chemical  
reactions in the flame. The effect of the combustor pressure on the fluid mechanics  
of the LSB flow field can be captured by its effect on the Reynolds number. As noted  
in Section 5.2, however, previous work indicated the Reynolds number may not be  
an important parameter for the LSB, particularly in the near field where the flame  
stabilization occurs. On the other hand, the effect of the combustor pressure on reac-  
tion rates in the flame is clearly important. Increasing the combustor pressure results  
in a lower laminar flame speed and reduced flame thickness for methane-air flames.  
According to the modified Damköhler model discussed earlier, the reduced laminar  
flame speed should have little or no effect on the flow field, since the contribution from  
 $S_L$  in Equation 5.1 is vanishingly small, even at the lowest reference velocities  
of our test conditions. However, as suggested by our discussion in Section 5.1, the  
validity of the simple model at elevated pressure conditions is questionable.

In order to resolve the uncertainties regarding how the LSB flame responds to  
combustor pressure, the flame was imaged over a range of operating conditions from  
3 to 12 atm. For these tests, the reference velocity and the equivalence ratio were  
held constant. However, the temperature of the reactants continues to increase with  
pressure. The reason for this was discussed in Chapter 3 and is attributable to the  
reduced heat losses in the connecting pipes at the high flow rates required to pressurize  
the LSB. The flame location and shape inferred from the flame images are presented  
in Figure 5.10.

At low to moderate pressures, the flame location is nearly invariant for  $S_{37^\circ}$ , but 1261  
moves upstream for the  $S_{45^\circ}$  cases. This behavior can be explained as follows. The 1262  
flame stabilization location for the  $S_{45^\circ}$  swirler is closer to the dump plane compared 1263  
to the  $S_{37^\circ}$  swirler. This should result in enhanced heat transfer to the dump plane 1264  
and consequently to the incoming reactants. This feedback is even more effective as 1265  
the temperature of the incoming reactants increases. This causes the upstream shift 1266  
of the  $S_{45^\circ}$  flame, while the  $S_{37^\circ}$  flame is less affected by these processes. 1267

At high pressures, however, both flames are observed to move downstream, despite 1268  
the increasing preheat temperatures. The apparent decrease in the turbulent flame 1269  
speed at these conditions is an unexpected result, and the modified Damköhler model 1270  
is insufficient in accounting for this observation. Figure FIXME also shows that the 1271  
flame angle for both cases decreases slightly with pressure. This suggests that the 1272  
turbulent flame speed was consistently decreasing with pressure. In light of this, 1273  
the nearly constant location of the  $S_{37^\circ}$  flame could be attributed to the effects of 1274  
increasing combustor pressure and preheat temperature nearly canceling each other 1275  
out at the lower pressures. 1276

## 5.6 Flame Structure 1277

**CHAPTER 6**  
**CONCLUSIONS**

1278

1279

## APPENDIX A

1280

### SEEDER DESIGN

1281

A new seeder was designed for use in high pressure implementations of diagnostic techniques like Laser Doppler Velocimetry (LDV), Particle Image Velocimetry (PIV), etc.

1282  
1283  
1284

The previous design, as shown in Figure A.1, was a fluidized bed seeding generator. Seeding particles in a cylindrical vessel are fluidized by an air-turbine vibrator. Air is introduced into the vessel in the form of two opposing jets directed tangentially to produce a small amount of swirl in the flow field. Particles are picked up by the air flow and the swirl aids in separating the heavy/coagulated clumps of seeding particles by centrifugal acceleration.

1285

1286

1287

1288

1289

1290

This design had several shortcomings. First, it is observed that the seeding density of the seeded flow generally decreases over time, even if the seeding particles have not been depleted. The seeding particles tend to coagulate over time, due to the buildup of moisture, static charge, etc. In such cases, the vibrator can no longer effectively fluidize the particles. Further, the tangential introduction of the air flow preferentially depletes particles near the walls of the container, leaving the center relatively undisturbed. The cumulative effect of these phenomena diminishes the effectiveness of the seeder.

1291

1292

1293

1294

1295

1296

1297

1298

Second, the fluidized bed requires a minimum amount of seeding particles to function effectively. This requires the seeder to be refilled even before all the seeding particles are consumed.

1299

1300

1301

Third, when designed for high pressure applications, the seeder will become quite heavy due to flanges and other fittings. Such a setup cannot be easily fluidized using a reasonable-sized air-turbine vibrator.

1302

1303

1304

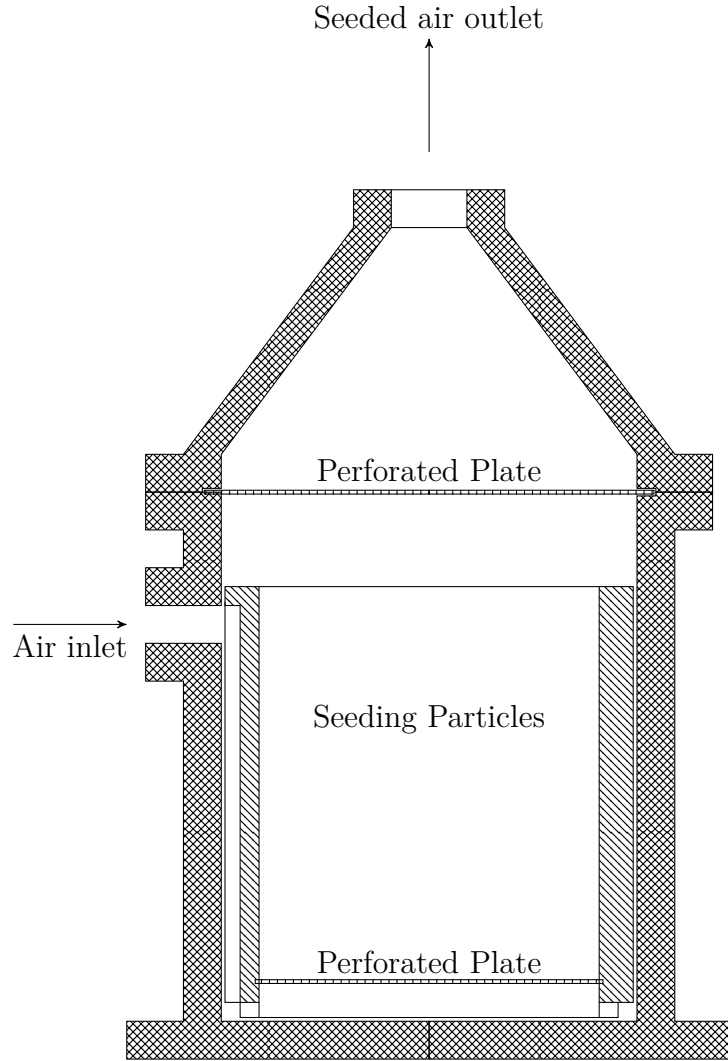


Figure A.1: A schematic of the old fluidized bed seeder is presented. The air enters the seeder through a groove along the inner vessel and is injected with a tangential velocity at the base of the seeder. The whole assembly is vibrated (vibrator not shown) to keep the particle bed fluidized. The seeded air flow exits through the outlet on the top.

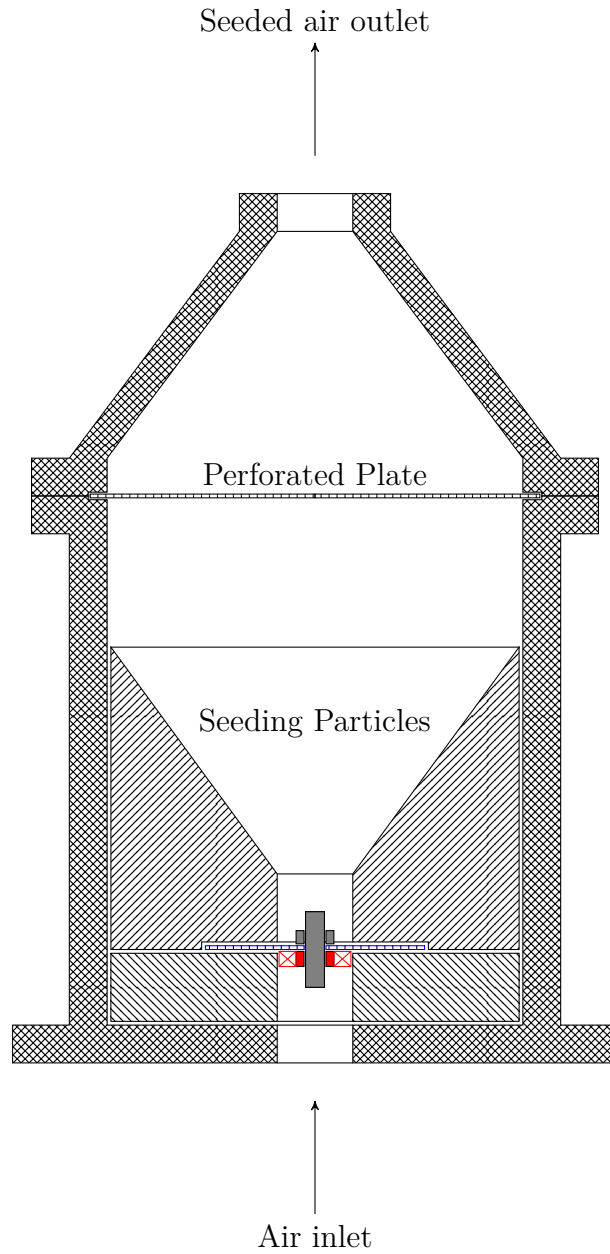


Figure A.2: *The improved design of the seeder is shown here in schematic form. The air enters the assembly from the inlet at the bottom, passes through the swirler (shown in red) and enters the seeder. The perforated plate at the bottom (shown in blue) keeps the seeding particles within the seeder. The swirler hub is threaded, allowing it to be secured to the perforated plate by a short steel bolt (shown in gray). After picking up the particles, a second perforated plate prevents large clumped seeding particles from passing through. The seeded air flow exits through the outlet at the top.*

The new seeder design is shown in Figure A.2, and resembles a funnel with a 1305  
swirler located halfway up the stem. A perforated base plate holds the swirler and 1306  
the seeding particles in the conical section of the swirler. Due to the steep angle of the 1307  
sides of the conical section, the seeding particles continuously collapse into the central 1308  
section. This negates any need for vibrating the system. Air is introduced from the 1309  
bottom of the seeder and enters the vessel by passing through the swirler. Since all 1310  
the air enters this way, there is a considerable amount of swirl in the resulting flow 1311  
field, Heavy/coagulated seeding particles are flung outward, while lighter particles are 1312  
carried with the air. After a sufficient distance to allow for the cyclonic separation 1313  
to be effective, the seeded air passes through another perforated plate which further 1314  
limits the presence of large clumps of particles. The exiting air is now spatially and 1315  
temporally uniformly seeded. 1316



## REFERENCES

1317

- [1] N. Syred and J. M. Beér, “Combustion in Swirling Flows: A Review,” *Combustion and Flame*, vol. 23, no. 2, pp. 143–201, 1974. 1318 1319
- [2] D. G. Lilley, “Swirl Flows in Combustion: A Review,” *AIAA Journal*, vol. 15, no. 8, pp. 1063–1078, 1977. 1320 1321
- [3] B. Bédard and R. K. Cheng, “Experimental Study of Premixed Flames in Intense Isotropic Turbulence,” *Combustion and Flame*, vol. 100, no. 3, pp. 485–494, 1995. 1322 1323
- [4] R. S. Barlow, R. W. Dibble, J. Y. Chen, and R. P. Lucht, “Effect of Damköhler Number on Superequilibrium OH Concentration in Turbulent Nonpremixed Jet Flames,” *Combustion and Flame*, vol. 82, no. 3-4, pp. 235–251, 1990. 1324 1325 1326
- [5] C. F. Kaminski, J. Hult, and M. Aldén, “High repetition rate planar laser induced fluorescence of OH in a turbulent non-premixed flame,” *Applied Physics B: Lasers and Optics*, vol. 68, no. 4, pp. 757–760, 1999. 1327 1328 1329
- [6] J. Hult, U. Meier, W. Meier, A. Harvey, and C. F. Kaminski, “Experimental analysis of local flame extinction in a turbulent jet diffusion flame by high repetition 2-D laser techniques and multi-scalar measurements,” in *Proceedings of the Combustion Institute*, vol. 30, pp. 701–709, 2005. 1330 1331 1332 1333
- [7] H. Malm, G. Sparr, J. Hult, and C. F. Kaminski, “Nonlinear diffusion filtering of images obtained by planar laser-induced fluorescence spectroscopy,” *Journal of The Optical Society of America A: Optics, image science, and vision*, vol. 17, no. 12, pp. 2148–2156, 2000. 1334 1335 1336 1337

- [8] R. Abu-Gharbieh, G. Hamarneh, T. Gustavsson, and C. F. Kaminski, “Flame front tracking by laser induced fluorescence spectroscopy and advanced image analysis,” *Optics Express*, vol. 8, no. 5, pp. 278–287, 2001.
- [9] C. M. Vagelopoulos and J. H. Frank, “An experimental and numerical study on the adequacy of CH as a flame marker in premixed methane flames,” in *Proceedings of the Combustion Institute*, vol. 30, pp. 241–249, 2005.
- [10] M. Köhler, A. Brockhinke, M. Braun-Unkhoff, and K. Kohse-Höinghaus, “Quantitative Laser Diagnostic and Modeling Study of C<sub>2</sub> and CH Chemistry in Combustion,” *The Journal of Physical Chemistry A*, vol. 114, no. 14, pp. 4719–4734, 2010.
- [11] C. P. Fenimore, “Formation of nitric oxide in premixed hydrocarbon flames,” in *Symposium (International) on Combustion*, vol. 13, pp. 373–380, 1971.
- [12] Z. S. Li, J. Kiefer, J. Zetterberg, M. Linvin, A. Leipertz, X. S. Bai, and M. Aldén, “Development of improved PLIF CH detection using an Alexandrite laser for single-shot investigation of turbulent and lean flames,” in *Proceedings of the Combustion Institute*, vol. 31, pp. 727–735, 2007.
- [13] H. N. Najm, P. H. Paul, C. J. Mueller, and P. S. Wyckoff, “On the Adequacy of Certain Experimental Observables as Measurements of Flame Burning Rate,” *Combustion and Flame*, vol. 113, no. 3, pp. 312–332, 1998.
- [14] J. Kiefer, Z. S. Li, J. Zetterberg, X. S. Bai, and M. Aldén, “Investigation of local flame structures and statistics in partially premixed turbulent jet flames using simultaneous single-shot CH and OH planar laser-induced fluorescence imaging,” *Combustion and Flame*, vol. 154, no. 4, pp. 802–818, 2008.

- [15] P. H. Paul and H. N. Najm, “Planar laser-induced fluorescence imaging of flame  
heat release rate,” in *Symposium (International) on Combustion*, vol. 27, pp. 43–  
50, 1998.
- [16] B. O. Ayoola, R. Balachandran, J. H. Frank, E. Mastorakos, and C. F. Kamin-  
ski, “Spatially resolved heat release rate measurements in turbulent premixed  
flames,” *Combustion and Flame*, vol. 144, no. 1, pp. 1–16, 2006.
- [17] J. Kiefer, Z. S. Li, T. Seeger, A. Leipertz, and M. Aldén, “Planar laser-induced  
fluorescence of HCO for instantaneous flame front imaging in hydrocarbon  
flames,” in *Proceedings of the Combustion Institute*, vol. 32, pp. 921–928, 2009.
- [18] C. K. Chan, K. S. Lau, W. K. Chin, and R. K. Cheng, “Freely propagating open  
premixed turbulent flames stabilized by swirl,” in *Symposium (International) on  
Combustion*, vol. 24, pp. 511–518, 1992.
- [19] R. K. Cheng, “Velocity and Scalar Characteristics of Premixed Turbulent Flames  
Stabilized by Weak Swirl,” *Combustion and Flame*, vol. 101, no. 1-2, pp. 1–14,  
1995.
- [20] T. Plessing, C. Kortschik, N. Peters, M. S. Mansour, and R. K. Cheng, “Measure-  
ments of the turbulent burning velocity and the structure of premixed flames on  
a low-swirl burner,” in *Proceedings of the Combustion Institute*, vol. 28, pp. 359–  
366, 2000.
- [21] I. G. Shepherd and R. K. Cheng, “The Burning Rate of Premixed Flames in  
Moderate and Intense Turbulence,” *Combustion and Flame*, vol. 127, no. 3,  
pp. 2066–2075, 2001.
- [22] R. K. Cheng, I. G. Shepherd, B. Bédard, and L. Talbot, “Premixed turbulent flame  
structures in moderate and intense isotropic turbulence,” *Combustion Science  
and Technology*, vol. 174, no. 1, pp. 29–59, 2002.

- [23] I. G. Shepherd, R. K. Cheng, T. Plessing, C. Kortschik, and N. Peters, “Premixed flame front structure in intense turbulence,” in *Proceedings of the Combustion Institute*, vol. 29, pp. 1833–1840, 2002.
- [24] C. Kortschik, T. Plessing, and N. Peters, “Laser optical investigation of turbulent transport of temperature ahead of the preheat zone in a premixed flame,” *Combustion and Flame*, vol. 136, no. 1-2, pp. 43–50, 2004.
- [25] L. P. H. de Goey, T. Plessing, R. T. E. Hermanns, and N. Peters, “Analysis of the flame thickness of turbulent flamelets in the thin reaction zones regime,” in *Proceedings of the Combustion Institute*, vol. 30, pp. 859–866, 2005.
- [26] J. B. Bell, R. K. Cheng, M. S. Day, and I. G. Shepherd, “Numerical simulation of Lewis number effects on lean premixed turbulent flames,” in *Proceedings of the Combustion Institute*, vol. 31, pp. 1309–1317, 2007.
- [27] D. T. Yegian and R. K. Cheng, “Development of a lean premixed low-swirl burner for low NO<sub>x</sub> practical applications,” *Combustion Science and Technology*, vol. 139, no. 1, pp. 207–227, 1998.
- [28] R. K. Cheng, D. T. Yegian, M. M. Miyasato, G. S. Samuelsen, C. E. Benson, R. Pellizzari, and P. Loftus, “Scaling and development of low-swirl burners for low-emission furnaces and boilers,” in *Proceedings of the Combustion Institute*, vol. 28, pp. 1305–1313, 2000.
- [29] D. Littlejohn, A. J. Majeski, S. Tonse, C. Castaldini, and R. K. Cheng, “Laboratory investigation of an ultralow NO<sub>x</sub> premixed combustion concept for industrial boilers,” in *Proceedings of the Combustion Institute*, vol. 29, pp. 1115–1121, 2002.
- [30] M. R. Johnson, D. Littlejohn, W. A. Nazeer, K. O. Smith, and R. K. Cheng, “A comparison of the flowfields and emissions of high-swirl injectors and low-

- swirl injectors for lean premixed gas turbines,” in *Proceedings of the Combustion Institute*, vol. 30, pp. 2867–2874, 2005. 1410 1411
- [31] W. A. Nazeer, K. O. Smith, P. Sheppard, R. K. Cheng, and D. Littlejohn, “Full scale testing of a low swirl fuel injector concept for ultra-low NO<sub>x</sub> gas turbine combustion systems,” in *Proceedings of ASME Turbo Expo GT2006-90150*, 2006. 1412 1413 1414
- [32] R. K. Cheng, D. Littlejohn, W. A. Nazeer, and K. O. Smith, “Laboratory studies of the flow field characteristics of low-swirl injectors for adaptation to fuel-flexible turbines,” in *Proceedings of ASME Turbo Expo GT2006-90878*, 2006. 1415 1416 1417
- [33] R. K. Cheng, D. Littlejohn, W. A. Nazeer, and K. O. Smith, “Laboratory Studies of the Flow Field Characteristics of Low-Swirl Injectors for Adaptation to Fuel-Flexible Turbines,” *Journal of Engineering for Gas Turbines and Power*, vol. 130, p. 021501, 2008. 1418 1419 1420 1421
- [34] R. K. Cheng and D. Littlejohn, “Effects of combustor geometry on the flowfields and flame properties of a low-swirl injector,” in *Proceedings of ASME Turbo Expo GT2008-50504*, 2008. 1422 1423 1424
- [35] R. K. Cheng and D. Littlejohn, “Laboratory Study of Premixed H<sub>2</sub>-Air and H<sub>2</sub>-N<sub>2</sub>-Air Flames in a Low-Swirl Injector for Ultralow Emissions Gas Turbines,” *Journal of Engineering for Gas Turbines and Power*, vol. 130, p. 031503, 2008. 1425 1426 1427
- [36] D. Littlejohn and R. K. Cheng, “Fuel effects on a low-swirl injector for lean premixed gas turbines,” in *Proceedings of the Combustion Institute*, vol. 31, pp. 3155–3162, 2007. 1428 1429 1430
- [37] R. K. Cheng, D. Littlejohn, P. A. Strakey, and T. Sidwell, “Laboratory investigations of a low-swirl injector with H<sub>2</sub> and CH<sub>4</sub> at gas turbine conditions,” in *Proceedings of the Combustion Institute*, vol. 32, pp. 3001–3009, 2009. 1431 1432 1433

- [38] D. Littlejohn, R. K. Cheng, D. R. Noble, and T. Lieuwen, “Laboratory Investiga- 1434  
tions of Low-Swirl Injectors Operating With Syngases,” *Journal of Engineering* 1435  
*for Gas Turbines and Power*, vol. 132, p. 011502, 2010. 1436
- [39] P. Petersson, J. Olofsson, C. Brackman, H. Seyfried, J. Zetterberg, M. Richter, 1437  
M. Aldén, M. A. Linne, R. K. Cheng, A. Nauert, D. Geyer, and A. Dreizler, 1438  
“Simultaneous PIV/OH-PLIF, Rayleigh thermometry/OH-PLIF and stereo PIV 1439  
measurements in a low-swirl flame,” *Applied Optics*, vol. 46, no. 19, pp. 3928– 1440  
3936, 2007. 1441
- [40] R. H. Barnes, C. E. Moeller, J. F. Kircher, and C. M. Verber, “Dye-Laser Excited 1442  
CH Flame Fluorescence,” *Applied Optics*, vol. 12, no. 11, pp. 2531–2532, 1973. 1443
- [41] J. F. Verdieck and P. A. Bonczyk, “Laser-induced saturated fluorescence in- 1444  
vestigations of CH, CN and NO in flames,” in *Symposium (International) on* 1445  
*Combustion*, vol. 18, pp. 1559–1566, 1981. 1446
- [42] M. G. Allen, R. D. Howe, and R. K. Hanson, “Digital imaging of reaction zones 1447  
in hydrocarbon-air flames using planar laser-induced fluorescence of CH and C<sub>2</sub>,” 1448  
*Optics Letters*, vol. 11, no. 3, pp. 126–128, 1986. 1449
- [43] M. Namazian, R. L. Schmitt, and M. B. Long, “Two-wavelength single laser CH 1450  
and CH<sub>4</sub> imaging in a lifted turbulent diffusion flame,” *Applied Optics*, vol. 27, 1451  
no. 17, pp. 3597–3600, 1986. 1452
- [44] R. W. Schefer, M. Namazian, and J. Kelly, “Stabilization of lifted turbulent-jet 1453  
flames,” *Combustion and Flame*, vol. 99, no. 1, pp. 75–86, 1994. 1454
- [45] P. H. Paul and J. E. Dec, “Imaging of reaction zones in hydrocarbon-air flames 1455  
by use of planar laser-induced fluorescence of CH,” *Optics Letters*, vol. 19, no. 13, 1456  
pp. 998–1000, 1994. 1457

- [46] C. D. Carter, J. M. Donbar, and J. F. Driscoll, “Simultaneous CH planar laser- 1458  
induced fluorescence and particle imaging velocimetry in turbulent nonpremixed 1459  
flames,” *Applied Physics B: Lasers and Optics*, vol. 66, no. 1, pp. 129–132, 1998. 1460
- [47] K. A. Watson, K. M. Lyons, J. M. Donbar, and C. D. Carter, “Observations 1461  
on the Leading Edge in Lifted Flame Stabilization,” *Combustion and Flame*, 1462  
vol. 119, no. 1-2, pp. 199–202, 1999. 1463
- [48] K. A. Watson, K. M. Lyons, J. M. Donbar, and C. D. Carter, “Simultaneous 1464  
Rayleigh Imaging and CH-PLIF Measurements in a Lifted Jet Diffusion Flame,” 1465  
*Combustion and Flame*, vol. 123, no. 1–2, pp. 252–265, 2000. 1466
- [49] J. M. Donbar, J. F. Driscoll, and C. D. Carter, “Reaction Zone Structure in 1467  
Turbulent Nonpremixed Jet Flames—From CH-OH PLIF Images,” *Combustion* 1468  
*and Flame*, vol. 122, no. 1-2, pp. 1–19, 2000. 1469
- [50] D. Han and M. G. Mungal, “Simultaneous measurement of velocity and CH layer 1470  
distribution in turbulent non-premixed flames,” in *Proceedings of the Combustion* 1471  
*Institute*, vol. 28, pp. 261–267, 2000. 1472
- [51] P. S. Kothnur, M. S. Tsurikov, N. T. Clemens, J. M. Donbar, and C. D. Carter, 1473  
“Planar imaging of CH, OH, and velocity in turbulent non-premixed jet flames,” 1474  
in *Proceedings of the Combustion Institute*, vol. 29, pp. 1921–1927, 2002. 1475
- [52] D. Han and M. G. Mungal, “Simultaneous measurements of velocity and CH 1476  
distributions. Part 1: jet flames in co-flow,” *Combustion and Flame*, vol. 132, 1477  
no. 3, pp. 565–590, 2003. 1478
- [53] D. Han and M. G. Mungal, “Simultaneous measurements of velocity and CH 1479  
distributions. Part II: deflected jet flames,” *Combustion and Flame*, vol. 133, 1480  
no. 1–2, pp. 1–17, 2003. 1481

- [54] J. A. Sutton and J. F. Driscoll, “Optimization of CH fluorescence diagnostics  
in flames: range of applicability and improvements with hydrogen addition,”  
*Applied Optics*, vol. 42, no. 15, pp. 2819–2828, 2003.
- [55] Z. S. Li, J. Zetterberg, M. Linvin, M. Aldén, J. Kiefer, T. Seeger, and A. Leipertz,  
“Planar laser-induced fluorescence of combustion intermediates in turbulent  
methane/air flames stabilized on a co-axial jet flame burner,” in *Proceedings  
of the European Combustion Meeting, ECM2007, Chania, Crete, Greece*, vol. 3,  
pp. 5–12–1–6, 2007.
- [56] J. Kiefer, Z. Li, J. Zetterberg, M. Linvin, and M. Aldén, “Simultaneous laser-  
induced fluorescence and sub-Doppler polarization spectroscopy of the CH radi-  
cal,” *Optics Communications*, vol. 270, no. 2, pp. 347–352, 2007.
- [57] Z. S. Li, M. Afzelius, J. Zetterberg, and M. Aldén, “Applications of a single-  
longitudinal-mode alexandrite laser for diagnostics of parameters of combustion  
interest,” *Review of Scientific Instruments*, vol. 75, no. 10, pp. 3208–3215, 2004.
- [58] A. C. Eckbreth, *Laser diagnostics for combustion temperature and species*. CRC,  
1996.
- [59] J. W. Daily, “Laser induced fluorescence spectroscopy in flames,” *Progress in  
Energy and Combustion Science*, vol. 23, no. 2, pp. 133–199, 1997.
- [60] J. Luque and D. R. Crosley, “Electronic transition moment and rotational transi-  
tion probabilities in CH. II.  $B^2\Sigma^- - X^2\Pi$  system,” *Journal of Chemical Physics*,  
vol. 104, no. 11, pp. 3907–3913, 1996.
- [61] N. L. Garland and D. R. Crosley, “Energy transfer processes in CH  $A^2\Delta$   
and  $B^2\Sigma^-$  in an atmospheric pressure flame,” *Applied Optics*, vol. 24, no. 23,  
pp. 4229–4237, 1985.



- [62] G. Richmond, M. L. Costen, and K. G. McKendrick, "Collision-Partner Depen- 1506  
dence of Energy Transfer between the CH  $A^2\Delta$  and  $B^2\Sigma^-$  States," *The Journal* 1507  
*of Physical Chemistry A*, vol. 109, no. 4, pp. 542–553, 2005. 1508
- [63] E. F. van Dischoeck, "Photodissociation processes in the CH molecule," *The* 1509  
*Journal of Chemical Physics*, vol. 86, no. 1, pp. 196–214, 1987. 1510
- [64] J. Luque, R. J. H. Klein-Douwel, J. B. Jeffries, and D. R. Crosley, "Collisional 1511  
processes near the CH  $B^2\Sigma^- v' = 0, 1$  predissociation limit in laser-induced fluo- 1512  
rescence flame diagnostics," *Applied Physics B: Lasers and Optics*, vol. 71, no. 1, 1513  
pp. 85–94, 2000. 1514
- [65] J. Luque and D. R. Crosley, "Electronic transition moment and rotational tran- 1515  
sition probabilities in CH. I.  $A^2\Delta - X^2\Pi$  system," *Journal of Chemical Physics*, 1516  
vol. 104, no. 6, pp. 2146–2155, 1996. 1517
- [66] A. Marshall, P. Venkateswaran, D. Noble, J. Seitzman, and T. Lieuwen, "Devel- 1518  
opment and characterization of a variable turbulence generation system," *Exper-* 1519  
*iments in Fluids*, vol. 51, no. 3, pp. 611–620, 2011. 1520
- [67] A. Melling, "Tracer particles and seeding for particle image velocimetry," *Mea-* 1521  
*surement Science and Technology*, vol. 8, no. 1, pp. 1406–1416, 1997. 1522
- [68] B. Hemmerling, "Beam steering effects in turbulent high-pressure flames," in 1523  
*Proceedings of SPIE*, vol. 3108, pp. 32–37, 1997. 1524
- [69] C. J. Dasch, "One-dimensional tomography: a comparison of abel, onion-peeling, 1525  
and filtered backprojection methods," *Applied Optics*, vol. 31, no. 8, pp. 1146– 1526  
1152, 1992. 1527

- [70] N. L. Garland and D. R. Crosley, “Relative transition probability measurements 1528  
in the  $A - X$  and  $B - X$  systems of CH,” *Journal of Quantitative Spectroscopy 1529  
and Radiative Transfer*, vol. 33, no. 6, pp. 591–595, 1985. 1530
- [71] M. Zachwieja, “New Investigations of the  $A^2\Delta - X^2\Pi$  Band System in the 1531  
CH Radical and a New Reduction of the Vibration-Rotation Spectrum of CH 1532  
from the ATMOS Spectra,” *Journal of Molecular Spectroscopy*, vol. 170, no. 2, 1533  
pp. 285–309, 1995. 1534
- [72] S. H. Stårner and R. W. Bilger, “Joint measurements of velocity and scalars in 1535  
turbulent diffusion flame with moderate swirl,” in *Symposium (International) on 1536  
Combustion*, vol. 21, pp. 1569–1577, 1986. 1537